

# High-resolution Transmission Spectroscopy of MASCARA-2 b with EXPRES

H. Jens Hoeijmakers<sup>1,2</sup>, Samuel H. C. Cabot<sup>3</sup>, Lily Zhao<sup>3</sup>, Lars A. Buchhave<sup>4</sup>, René Tronsgaard<sup>4</sup>, Daniel Kitzmann<sup>2</sup>, Simon L. Grimm<sup>2</sup>, Heather M. Cegla<sup>1</sup>, Vincent Bourrier<sup>1</sup>, David Ehrenreich<sup>1</sup>, Kevin Heng<sup>2,5</sup>, Christophe Lovis<sup>1</sup>, and Debra A. Fischer<sup>3</sup>

<sup>1</sup> Observatoire de Genève, Chemin des Maillettes 51, 1290, Versoix, Switzerland

<sup>2</sup> Center for Space and Habitability, Universität Bern, Gesellschaftsstrasse 6, 3012 Bern, Switzerland

<sup>3</sup> Yale University, 52 Hillhouse, New Haven, CT 06511, USA

<sup>4</sup> DTU Space, National Space Institute, Technical University of Denmark, Elektrovej 328, DK-2800 Kgs. Lyngby, Denmark

<sup>5</sup> University of Warwick, Department of Physics, Astronomy & Astrophysics Group, Coventry CV4 7AL, United Kingdom

Received January 2, 2020; accepted April 17, 2020

## ABSTRACT

We report detections of atomic species in the atmosphere of MASCARA-2 b, using the first transit observations obtained with the newly commissioned EXPRES spectrograph. EXPRES is a highly stabilised optical echelle spectrograph, designed to detect stellar reflex motions with amplitudes down to 30 cm/s, and was recently deployed at the Lowell Discovery Telescope. By analysing the transmission spectrum of the ultra-hot Jupiter MASCARA-2 b using the cross-correlation method, we confirm previous detections of Fe I, Fe II and Na I, which likely originate in the upper regions of the inflated atmosphere. In addition, we report significant detections of Mg I and Cr II. The absorption strengths change slightly with time, possibly indicating different temperatures and chemistry in the day-side and night-side terminators. Using the effective stellar line-shape variation induced by the transiting planet, we constrain the projected spin-orbit misalignment of the system to  $1.6 \pm 3.1$  degrees, consistent with an aligned orbit. We demonstrate that EXPRES joins a suite of instruments capable of phase-resolved spectroscopy of exoplanet atmospheres.

## 1. Introduction

The emergence of a new generation of spectrographs opens avenues for detecting and characterizing exoplanets and their atmospheres with unprecedented fidelity. Exoplanets can be detected with high-resolution spectrographs due to their gravitational interaction with the host-star, causing a periodic Doppler shift in the observed stellar spectrum as the planet orbits. These measurements yield a lower limit to the mass of the planet or the mass itself if the planet orbits in an aligned plane that carries it through transit as seen from Earth. One may constrain the composition of a transiting planet by also measuring its radius, which then yields the mean density. Recent years have seen extensive efforts to develop a new generation of environmentally-controlled high-resolution spectrographs that provide ever increasing radial velocity (RV) precision and stability, to allow for more precise mass measurements, and for the detection of less massive planets further away from their host star. Indeed, several purpose-built instruments have come online in recent years. ESPRESSO (Pepe et al. 2013) was commissioned at the Very Large Telescope (VLT) in December 2017. HARPS-N/GIANO (Cosentino et al. 2012; Claudi et al. 2017; Oliva et al. 2018) at Telescopio Nazionale Galileo, CARMENES (Quirrenbach et al. 2010) at Calar Alto Observatory and SPIRou (Thibault et al. 2012) at the Canada France Hawaii Telescope provide high-resolution optical and NIR coverage. NIRPS (Wildi et al. 2017) at the ESO's 3.6-m telescope at La Silla and HARPS3 (Thom-

son et al. 2016) at the Isaac Newton Telescope are currently under development.

The EXtreme PREcision Spectrograph (EXPRES) was commissioned at the Lowell Observatory 4.3-m Lowell Discovery Telescope (LDT, Levine et al. 2012) in 2018. EXPRES is a vacuum-stabilized, fiber-fed,  $R \sim 140,000$ , optical spectrograph with wavelength calibration from a Menlo Systems laser frequency comb (LFC). It is optimized for wavelengths between 380 and 680 nm. The design goal of EXPRES was a RV precision of  $\sim 30 \text{ cm s}^{-1}$  on bright ( $V < 8$ ) main sequence stars. Observations with the LFC demonstrate an instrumental stability of  $7 \text{ cm s}^{-1}$  and formal errors of about  $25 \text{ cm s}^{-1}$  for an SNR of 250 when observing bright stars (Blackman et al. 2019; Petersburg et al. 2020).

High resolution spectrographs are able to directly probe spectral features in the atmospheres of exoplanets (Snellen et al. 2008). The high spectral resolution allows for individual spectral lines in the planet's spectrum to be resolved and provides measurements of the line-shape and depth (e.g. Redfield et al. 2008; Wyttenbach et al. 2015; Jensen et al. 2012; Khalafinejad et al. 2017; Wyttenbach et al. 2017; Allart et al. 2019; Seidel et al. 2019). The orbital velocity of hot-Jupiters is often in excess of  $100 \text{ km s}^{-1}$ . At  $R \sim 10^5$ , this motion is resolved in time-series exposures of a several-hour transit. Separating the spectrum of the planet from the host star using this Doppler shift was first applied to detect absorption by atmospheric CO in the infra-red transmission spectrum of HD 209458 b (Snellen et al. 2010). Later efforts employed this technique to detect the thermal emission of

both transiting and non-transiting hot-Jupiters, resulting in detections of CO, H<sub>2</sub>O, CH<sub>4</sub> and HCN (e.g. Brogi et al. 2012; Birkby et al. 2013; Lockwood et al. 2014; Brogi et al. 2016; Piskorz et al. 2016; Birkby et al. 2017; Hawker et al. 2018; Cabot et al. 2019; Guilluy et al. 2019; Flagg et al. 2019). The technique has also been applied at optical wavelengths to detect TiO in the day-side spectrum of WASP-33 b using the HDS/Subaru instrument (Nugroho et al. 2017), and atomic metal lines in the transmission spectrum of KELT-9 b (Hoeijmakers et al. 2018a, 2019) using HARPS-N/*TNG* and PEPSI/*LBT* (Cauley et al. 2019). Ongoing improvements in resolution, stability, and wavelength calibration will enable more detailed detections of chemistry and atmospheric dynamics for a multitude of exoplanet systems (Heng & Showman 2015; Crossfield 2015; Madhusudhan et al. 2016; Birkby 2018; Triad 2018; Wright 2018). As such, stabilized, fiber-fed high-resolution spectrographs have a complementary dual-use in the discovery of exoplanets as well as the characterization of their atmospheres.

MASCARA-2 b/Kelt-20 b (hereafter M2) was independently discovered by the Multi-site All-Sky CAmERA (MASCARA) (Talens et al. 2018) and the Kilo-degree Extremely Little Telescope (KELT) (Lund et al. 2017), which both survey bright stars for signs of periodically transiting exoplanets. The planet is a hot-Jupiter, transiting the bright ( $m_V = 7.6$ ) A2 main sequence star HD 185603 in a 3.47 day orbit. The orbit of the planet is aligned, which is not common for this type of star (Winn et al. 2010; Schlaufman 2010; Albrecht et al. 2012). Strong irradiation from its host star gives M2 b a high equilibrium temperature of  $T_{eq} \sim 2260$  K, placing it in the extreme class of ultra-hot Jupiters. Several such planets have been studied to date, most notably KELT-9 b, which, with  $T_{eq} = 4050$  K is the hottest known planet around a main-sequence star. In light of previous detections of atomic metals in KELT-9 b (Hoeijmakers et al. 2018a, 2019), atmospheric studies of other ultra-hot Jupiters warrant searches for vaporized metals and ions.

The transmission spectrum of M2 has been observed extensively with the HARPS-N and CARMENES spectrographs, leading to detections of two Balmer lines of hydrogen, the Na I D-lines, the Ca II infra-red triplet, Fe I, Fe II and tentative evidence for an Mg I line at 517.268 (Casasayas-Barris et al. 2018, 2019; Nugroho et al. 2020; Stangret et al. 2020). These detections are indicative of the high temperatures prevalent at the day-side and terminator regions. The detection of strong hydrogen absorption may further be indicative of an extended or evaporating atmosphere (Yan & Henning 2018; Turner et al. 2020).

This paper presents the results of one night of transit observations of M2 with the EXPRES instrument, which constitute the first application of EXPRES for the purpose of exoplanet transit transmission spectroscopy. With these observations, we aim to demonstrate that EXPRES offers significant potential for atmospheric characterization in addition to its main purpose of RV monitoring for exoplanet discovery. The paper is organized as follows: in section 2 we describe the observations and present our analysis of the transmission spectra. In section 3, we discuss our results, including analysis of the Doppler shadow induced by the Rossiter-McLaughlin effect. We detect spectroscopic signatures of the atmosphere of M2 by confirming the presence of Fe I and Fe II (Casasayas-Barris et al. 2019; Nugroho et al. 2020; Stangret et al. 2020), and presenting strong evidence

for Mg I, Na I and Cr II. We summarize our results in Section 4.

## 2. Transit observations of MASCARA-2 b

A single transit of M2 was observed with the LDT during the night of June 1, 2018. The night was clear with an average seeing of approximately 1."2. The observations lasted from 09:03 to 14:23 UTC, with a total of 68 exposures of the system, of which 51 were obtained in-transit (we include ingress/egress in our in-transit sample). The signal to noise ratio for these exposures reached approximately 40-50 near 5000 Å throughout the night. Most exposures were approximately 200 seconds, while 15-minute exposures at the start of the night provided high S/N out-of-transit spectra.

Wavelength calibration is carried out with a Menlo Systems Laser Frequency Comb as well as a ThAr line-lamp. Exposures are taken through the science fiber and are interspersed with science observations approximately every 30 minutes. A tune-able LED is used to take flat-fields. Sets of zero-second bias frames are taken before and after the observing night, and dark current is corrected using the CCD overscan regions. We perform extractions with the *RePack*<sup>1</sup> code, adapted from a version purposed for use with HARPS-N data products (Fischer et al. 2016). We also divide spectra by a blaze-function derived from flat-field calibrations. The result is a pipeline-reduced spectral time series in Earth's rest-frame, shown in the top panel of Figure 1.

Our subsequent analysis follows the approach of Hoeijmakers et al. (2019) that resulted in the detections of iron and titanium in the atmosphere of KELT-9 b, using a similar sequence of observations by the HARPS-N spectrograph. The cross-correlation procedure discussed below differs from the approach used by Casasayas-Barris et al. (2018, 2019), which was based on the direct analysis of individual absorption lines in a single, co-added transmission spectrum.

### 2.1. Telluric Correction and Detrending

Absorption lines from the stellar photosphere as well as the Earth's atmosphere (telluric lines) are the most dominant spectral features in the observed spectra. We model the telluric contamination in each spectrum with the *Molecfit* package (Smette et al. 2015). *Molecfit* processes an observed spectrum along with ambient weather, time, and location information to model the structure of the Earth's atmosphere during an observation and to fit a line-by-line radiative transfer model to the spectrum. We use similar initial parameters to those used by Allart et al. (2017), such as the atmospheric profile, degree of the continuum and wavelength polynomial fits, and resolution fit kernel. We chose more relaxed convergence tolerances of  $10^{-5}$ , which improved runtime and the quality of fit. Because M2 is a fast rotator, most stellar lines are significantly broadened and blended to form a quasi-continuum, minimizing their effect on the fit of individual telluric lines. We fit each spectrum in the time-series individually and divide the spectrum by the fit to remove tellurics (Figure 1, middle and bottom panels).

<sup>1</sup> Written by Lars Buchhave

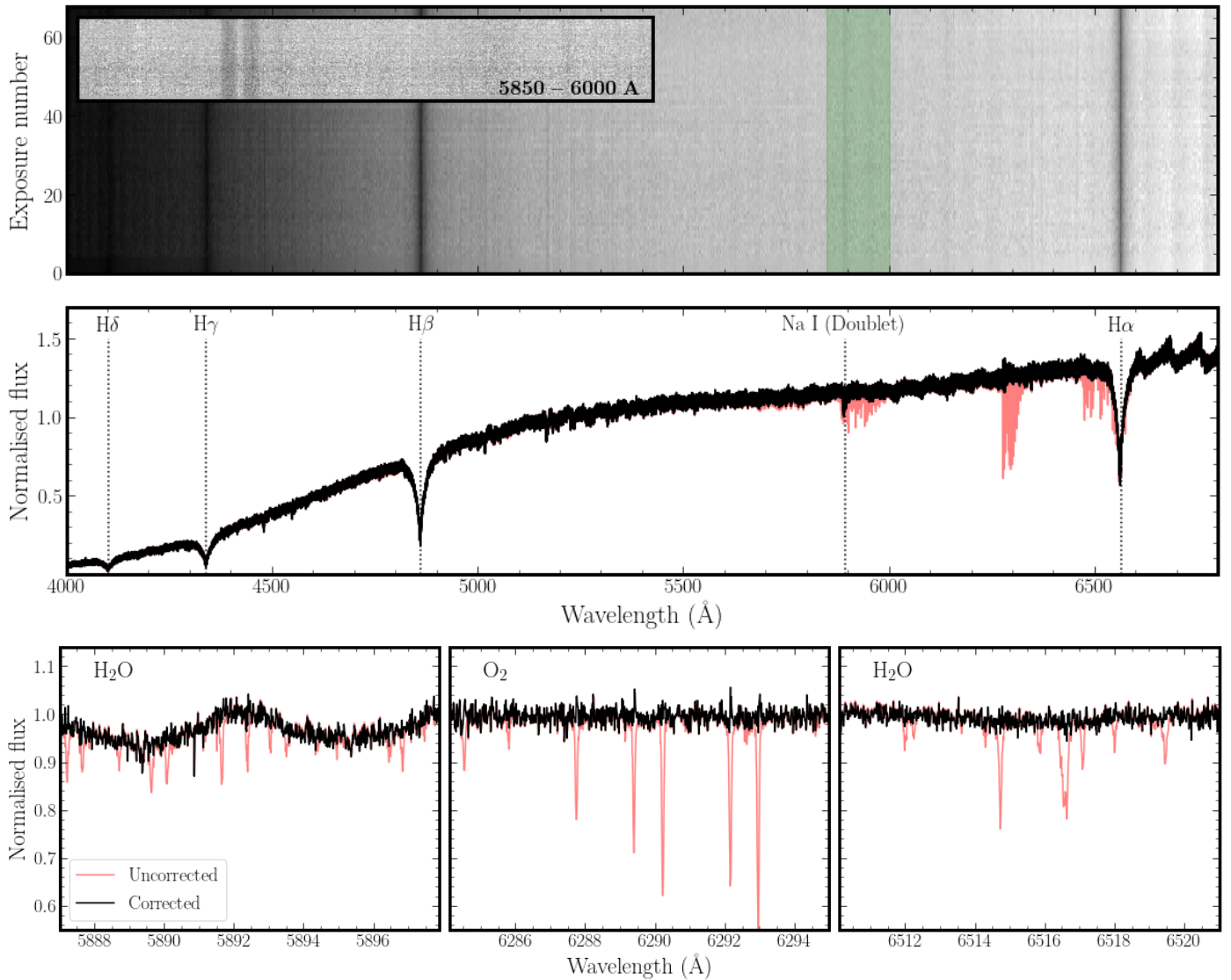


**Fig. 1.** Spectra obtained on June 1, 2018 with EXPRES. *Top Panel:* Time-series, high-resolution spectra cleaned and corrected for tellurics. The orders are stitched together for visualization, but are analyzed independently during cross-correlation. Common features such as stellar lines appear as dark columns. *Inlet:* Zoom-in of the time-series spectra between 5850-6000 Å (marked by the green band), revealing the broadened Na doublet. *Middle Panel:* Example 1-dimensional spectrum from the time-series, before (red) and after (black) telluric correction. The features around 6700 Å are an artifact of order stitching. Some strong stellar lines, including the Balmer series and the Sodium D lines are marked. *Bottom Panels:* Zoom-in of the example 1-dimensional spectrum, demonstrating the effect telluric correction in strongly contaminated regions (due to H<sub>2</sub>O, O<sub>2</sub> and H<sub>2</sub>O, from left to right).

Our analysis uses spectra in the wavelength range 4000-6800 Å. Bluer wavelengths are subject to very low instrumental throughput, and redder wavelengths suffer severe telluric contamination that is more difficult to model while covering comparatively few atomic metal lines. This leaves 64 out of 88 orders, which are treated separately until combining their individual cross-correlation functions at the end of the analysis. For computational reasons, we resample all of the spectra onto a common wavelength grid of 0.01 Å spacing. We identify bad pixels (e.g. due to cosmic ray hits) by selecting  $5\sigma$  outliers in a sliding 500 pixel window, and setting them to the mean of the values in the window. We shift each spectrum into the rest-frame of the star, taking into account the  $-21.07 \text{ km s}^{-1}$  systemic velocity (denoted  $V_{\text{sys}}$ ) (Talens et al. 2018) and the Barycentric Earth Radial Velocity (BERV) correction (calculated using the *Astropy* package, see Astropy Collaboration et al.

2013; Price-Whelan et al. 2018). The BERV changes by  $\lesssim 1 \text{ km s}^{-1}$  over the course of the transit. We do not correct for stellar reflex motion. This effect is negligible because M2 has broad absorption lines due to its fast rotation. We note the presence of excess absorption in the cores of the Na doublet which we attribute to stationary ISM absorption, as seen in previous analyses of M2 (Casasayas-Barris et al. 2018, 2019). As in these studies, neglecting the stellar reflex correction helps ensure the excess absorption cancels during division by the master out-of-transit spectrum (see below). The 2.5% of pixels on either end of each order are masked from cross-correlation. This step removes edge artifacts from shifting to the stellar rest-frame, as well as pixels with low flux located at the edges of the blaze function.

We co-add all out-of-transit spectra  $\{f_t\}_{t \in t_{\text{out}}}$  to obtain a master spectrum of the star  $F_{\text{out}}$ . We subsequently compute individual transmission spectra  $\{\tilde{r}_t\}_{t \in t_{\text{in}}}$  by divid-

ing each in-transit spectrum  $\{f_t\}_{t \in t_{\text{in}}}$  by  $F_{\text{out}}$  (Wytenbach et al. 2015; Allart et al. 2017; Hoeijmakers et al. 2018a; Casasayas-Barris et al. 2018, 2019). Finally, we apply a high-pass Gaussian filter with 75 pixel standard-deviation and subtract from the pixels in each wavelength bin their time-average, removing broad-band variations (Hoeijmakers et al. 2018b).

## 2.2. Cross-correlation

Atomic or molecular species present in the exoplanet atmosphere may cause thousands of individual absorption lines in the atmospheric transmission spectrum. Cross-correlating the spectra with a model template spectrum combines the contributions of all these lines to reduce the photon-noise and yield significant detections of these elements (Snellen et al. 2010). We use high-resolution model spectra for Na I, Mg I, Sc I, Sc II, Ti I, Ti II, Cr I, Cr II, Fe I, Fe II and Y II using opacities computed with HELIOS-K (Grimm & Heng 2015) and equilibrium chemistry at  $T = 4,000$  K with FastChem (Stock et al. 2018). These templates resulted in detections in the analysis of the transmission spectrum of KELT-9 b by Hoeijmakers et al. (2019), who provide a detailed description of their construction. These templates are publicly accessible via the CDS <sup>2</sup>.

To compute the cross-correlation, we apply Doppler shifts of  $-500$  to  $500$  km s<sup>-1</sup> to the template in increments of  $1.0$  km s<sup>-1</sup>. At each velocity  $v$ , and for a given transmission spectrum  $\tilde{r}_t$ , we take the weighted average of values in the spectrum. The weights are a product of the Doppler-shifted template, which is zero everywhere except at locations of line transitions, and the inverse of each wavelength bin's time-variance, which reduces the contribution of noisy pixels (Brogi et al. 2016). This procedure yields a cross-correlation function (CCF) as a function of velocity and time, which contains the average line-strength of features in the transmission spectrum (Hoeijmakers et al. 2019).

## 2.3. Rossiter-McLaughlin effect

The orbit of M2 b is aligned (Lund et al. 2017; Talens et al. 2018), meaning that the planet obscures the blue-shifted part of the star at the start of the transit, and moves to the red-shifted part towards egress. This passage across the stellar disk changes the shapes of the disk-integrated, rotation-broadened stellar absorption lines, which gives rise to the Rossiter-McLaughlin (RM) effect seen in the RV measurements of the star during transit (Ohta et al. 2005). For a fast rotator like M2, broadened spectral features decrease the precision of RV measurements, making the RM effect difficult to resolve. However, when dividing the mean out-of-transit spectrum from each of the exposures, the line-deformation causes the stellar lines to be over-corrected at the instantaneous velocity of the obscured part of the stellar disk. This effect is known as the "Doppler shadow" that is cast by the planet as it progresses through transit (Collier Cameron et al. 2010). The centroid velocity  $v_*(t)$  of the obscured stellar surface depends on the projected location of the planet with respect to the stellar spin axis, which changes over time as the planet progresses through transit, and is described by the following analytical expressions

(Collier Cameron et al. 2010; Bourrier et al. 2015), ignoring differential rotation of the stellar surface and convective blueshift (Cegla et al. 2016):

$$v_*(t) = x_{\perp}(t)v_{\text{eq}} \sin i_* \quad (1)$$

where  $v_{\text{eq}} \sin i_*$  is the projected equatorial rotation velocity of the star, and  $x_{\perp}$  is the orthogonal distance of the obscured region to the projected spin axis:

$$x_{\perp}(t) = x_p(t) \cos(\lambda) - y_p(t) \sin(\lambda) \quad (2)$$

where  $\lambda$  is the spin-orbit misalignment and  $x_p(t)$  and  $y_p(t)$  are the coordinates of the planet:

$$x_p(t) = \frac{a}{R_*} \sin(2\pi\phi) \quad (3)$$

$$y_p(t) = -\frac{a}{R_*} \cos(2\pi\phi) \cos(i_p) \quad (4)$$

with  $a$  the semi-major axis,  $R_*$  the radius of the star,  $i_p$  the orbital inclination,  $\phi$  the orbital phase at time  $t$  and the orbital inclination  $i_p$ .

The Doppler shadow is retrieved by cross-correlating the transmission spectra  $\{\tilde{r}_t\}_{t \in t_{\text{in}}}$  with a model template of the stellar spectrum. This template consists of a PHOENIX photosphere model spectrum at a temperature of 9000 K and solar metallicity, obtained from the online PHOENIX library (Husser et al. 2013). The baseline of the template is subtracted via a high-pass filter so that it contains only the absorption lines with relative depths corresponding to the relative absorption of continuum radiation at each wavelength (i.e. continuum normalization).

The resulting two-dimensional CCF contains the signature of the Doppler shadow (see the top panel in Figure 2), from which the misalignment  $\lambda$  between the orbital plane of the planet and the projected stellar spin axis can be derived as is done when applying Doppler tomography (Collier Cameron et al. 2010) or the "Reloaded RM-effect" (Cegla et al. 2016). The shadow also overlaps with the expected RV of the planet, so it needs to be corrected before the signature of the planet atmosphere may be isolated (see the second panel, "RM RV Model", in Figure 2; the local obstructed RV overlaps the planetary RV, given by dashed and dotted lines respectively). We construct a model of the two-dimensional cross-correlation residual from the parameters of the Gaussian fits used to measure  $\lambda$ , following the approach by Hoeijmakers et al. (2018a). This model is scaled to minimize the sum of the squared residual when subtracting it from cross-correlation functions with other the templates used in this analysis (see third and fourth panels, "Shadow Model" and "Residual", in Figure 2). The Doppler shadow shows small variations in strength throughout the transit; darker regions are roughly correlated with higher exposure S/N. However, our empirical model is agnostic to the origin of these variations, and successfully removes the shadow to isolate the atmospheric absorption. The overlap region between the atmospheric absorption trail and the Doppler shadow may affect the co-added absorption signal; however, as described by Hoeijmakers et al. (2018a), the fit of Doppler shadow model ignores the overlap region and

<sup>2</sup> <https://cdsarc.unistra.fr/viz-bin/cat?J/A+A/627/A165>

enforces smoothly varying model parameters, which helps to preserve information at velocities for which the Doppler shadow and the planet absorption features overlap. This is possible because range of radial velocities spanned by the Doppler shadow differs significantly different from those of the planet atmosphere, due to the fast rotation of the host star.

#### 2.4. The time-averaged CCF

The planet's apparent RV is described by:

$$v(t) = K_p \sin(2\pi\phi(t)) + V_{\text{sys}} \quad (5)$$

where  $K_p$  is the planetary semi-amplitude. Note that since we shifted all spectra to the stellar rest-frame, the  $V_{\text{sys}}$  term above is set to  $0.0 \text{ km s}^{-1}$ . The orbital period  $P = 3.474119$  days and reference mid-transit time  $T_0 = 57909.0875$  MJD (Talens et al. 2018) determine the orbital phase,  $\phi(t)$  at the time of each exposure. We sample potential values for  $K_p$  from a grid ranging from  $0$ – $300 \text{ km s}^{-1}$  in steps of  $1.0 \text{ km s}^{-1}$  and shift each CCF by  $-K_p \sin(2\pi\phi(t))$ . At the true value of  $K_p$ , the CCFs are shifted into the rest frame of the planet, and may be optimally co-added to yield the time-average of the CCFs as a function of the systemic velocity  $V_{\text{sys}}$ . The planet signal is expected to occur at  $0.0 \text{ km s}^{-1}$  because the spectra have been shifted to the stellar rest-frame. In this way, we construct a two-dimensional map of the co-added cross-correlation signal at different combinations of  $K_p$  and  $V_{\text{sys}}$ , which has been termed the  $K_p V_{\text{sys}}$  diagram (Brogi et al. 2012). A statistically significant signal at the correct combination of  $K_p$  and  $V_{\text{sys}}$  confirms the presence of the model species in the atmosphere of the planet (Brogi et al. 2012). Additionally, we can examine a single row in this map that corresponds to any particular choice of  $K_p$ . The peak in this co-added CCF corresponds to the weighted mean of the depths of the absorption lines in the chosen rest-frame (Pino et al. 2018; Hoeijmakers et al. 2019). The orbital period and semi-major axis of M2 (Talens et al. 2018) and previous atmospheric measurements (Casasayas-Barris et al. 2019; Nugroho et al. 2020; Stangret et al. 2020) place  $K_p$  roughly between  $160$ – $190 \text{ km s}^{-1}$ .

### 3. Results

#### 3.1. Spin-orbit misalignment

By making use of the fact that the RV variation of the Doppler shadow traces the obscured area of the stellar disk as the planet moves through transit, the system architecture can be derived (Collier Cameron et al. 2010). To this end, we normalize the two-dimensional CCF by the expected flux decrease during the planet transit (i.e. the transit light-curve) and fit the centroid position of the correlation excess with a Gaussian profile in the cross-correlation function of each exposure, following Cegla et al. (2016) (see Fig. 3). We take the centroid  $v_*^{\text{obs}}(t)$  and its uncertainty  $\sigma_v^{\text{obs}}(t)$  as our measurement of the average RV of the occulted stellar surface. That is,  $v_*^{\text{obs}}(t)$  represents the measurement of  $v_*(t)$  which is defined in Equation 1. We assume a standard Gaussian log-likelihood function,

$$\mathcal{L} \propto -\frac{1}{2} \sum_t \left( \frac{v_*^{\text{obs}}(t) - \hat{v}_*(t)}{\sigma_v^{\text{obs}}(t)} \right)^2 \quad (6)$$

where  $\hat{v}_*(t)$  is the model-predicted value of  $v_*(t)$ . We subsequently perform a Markov Chain Monte Carlo (MCMC) analysis of the Doppler shadow to constrain orbital parameters of the system.

We assume Gaussian priors on each of the orbital parameters, with mean and standard deviation as reported by Talens et al. (2018) (see Table A.1). Our model contains 5 parameters: scaled semi-major axis  $a/R_*$ , projected obliquity  $\lambda$ , orbital inclination  $i_p$ , projected stellar rotation speed  $v \sin i_*$ , and a systematic RV offset to account for errors in the systemic velocity. We place a Gaussian prior on the offset with mean and standard deviation of  $0.0$  and  $5.0 \text{ km s}^{-1}$  respectively. The MCMC is performed with the `emcee` package (Foreman-Mackey et al. 2013), using 20 independent chains, each taking  $1 \times 10^5$  steps. Visual inspection of the chains suggests a burn-in time of  $\sim 200$  steps, and an auto-correlation length of  $\sim 3$  steps. We exclude the first 5000 steps of each chain and nine out of every ten remaining steps, and subsequently merge the chains, leaving  $> 10^5$  independent samples of the posterior. Correlation diagrams and histograms of each parameter are shown in Figure A.1, and the median values are quoted in Table A.1. Our results are generally consistent with Talens et al. (2018) and Lund et al. (2017). The marginalized distributions reduce the  $1\sigma$  uncertainty in  $v \sin i_*$  to  $< 1 \text{ km s}^{-1}$ , slightly improve constraints on  $\lambda$ , and constrain an absolute RV offset to within a few  $\text{km s}^{-1}$ . Distributions for  $a/R_*$  and  $i_p$  are dominated by the choice of priors, which are provided by the already tight constraints derived from transit photometry (Talens et al. 2018). Our best-fit parameters, in combination with Equations 1-4, and the orbital phase of each exposure, trace the path of the Doppler shadow (second panel, "RM RV Model", Figure 2). Importantly, we note a degeneracy between RV offset and  $\lambda$ , which highlights the need for precise measurements of  $V_{\text{sys}}$  when fitting for the spin-orbit misalignment. However, it is difficult to accurately measure  $V_{\text{sys}}$  for fast-rotators like M2, and literature estimates vary by several  $\text{km s}^{-1}$ .

#### 3.2. Transmission spectrum and cross-correlation

We present new detections of Cr II ( $4.1\sigma$ ) and Mg I ( $4.0\sigma$ ) in the atmosphere of M2 b, in addition to confirmations of Fe I ( $4.7\sigma$ ), Fe II ( $4.8\sigma$ ) and Na I ( $4.4\sigma$ ) (Casasayas-Barris et al. 2019; Nugroho et al. 2020; Stangret et al. 2020). The cross-correlation procedure and detection of Fe II is shown in Figure 4; the same plots for the remaining species are in the Appendix.

Several metrics have previously been used to determine detection significance in cross-correlation functions, including the amplitude of the CCF peak relative to the standard deviation of noise in the baseline of the CCF (Brogi et al. 2012), a Welch t-Test comparing distributions in the two-dimensional CCF (Birkby et al. 2017), and the uncertainty in a Gaussian fit to the CCF feature (Hoeijmakers et al. 2019). The significances determined in the present work represent the false-alarm probability (FAP) of detecting a comparable CCF enhancement by chance. We discuss FAP calculation in the following section. Summary statistics for each detected species, including the CCF peak, Gaussian fit, and FAP are listed in Table 1.

Our best-fit relative depth of Fe II ( $0.013 \pm 0.002\%$ ) is consistent with the  $0.08 \pm 0.04\%$  depth of individual

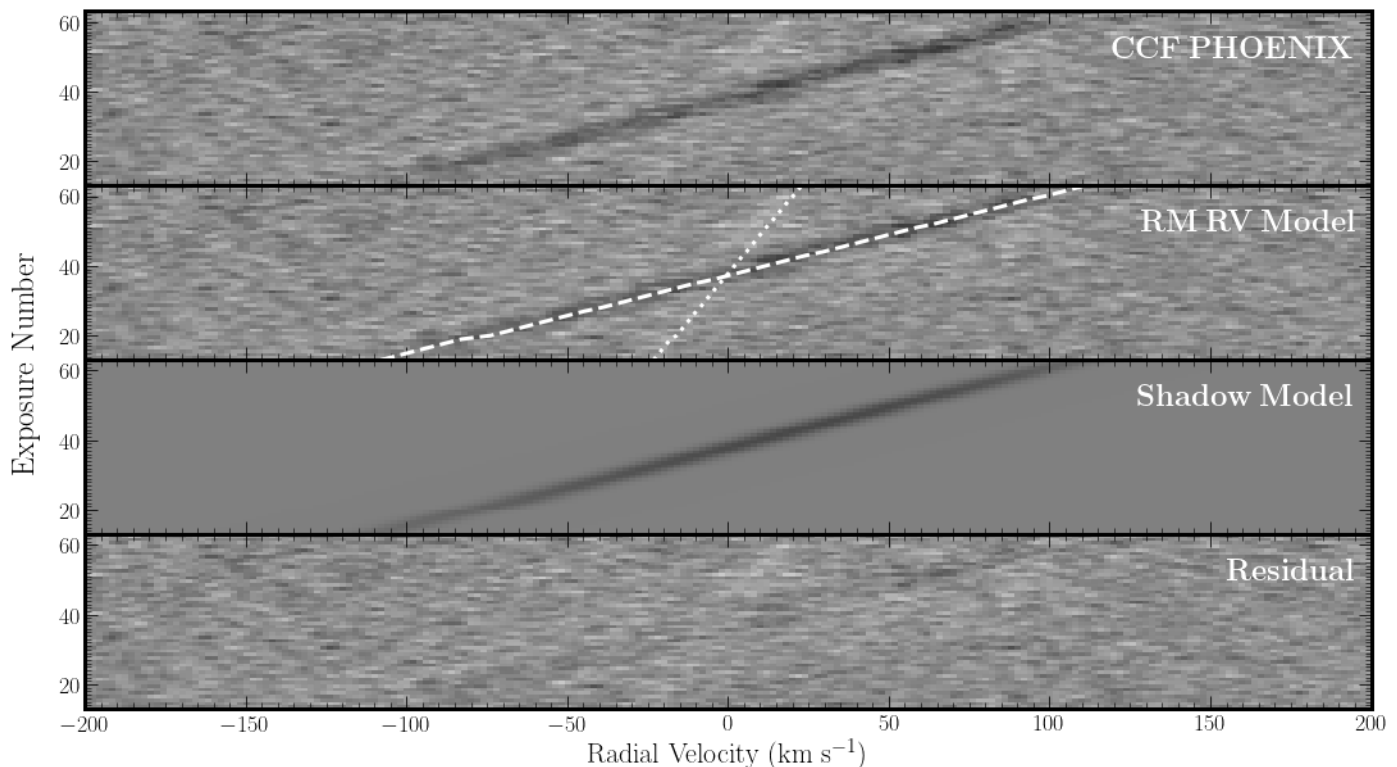


**Fig. 2.** Removal of the Doppler shadow caused by the transiting planet, from start of ingress to end of egress. *Top panel:* The cross-correlation of the exposures in-transit with a template constructed from a PHOENIX stellar photosphere model. *Second panel:* Same as top panel, annotated with the predicted RV of the occulted stellar region responsible for the Doppler shadow (dashed line). Also shown is the expected RV of the planet (dotted line) expected from the system parameters by (Lund et al. 2017; Talens et al. 2018). *Third Panel:* The model of the Doppler shadow, obtained by fitting a Gaussian profile to the shadow feature in each of the in-transit cross-correlation functions. *Bottom panel:* Residuals after subtraction.

Species	CCF <sub>max</sub> (%)	S/N	$v_{\text{CCF}}$ (km s <sup>-1</sup> )	$A$ (%)	$\mu$ (km s <sup>-1</sup> )	FWHM (km s <sup>-1</sup> )	$p_{\text{FAP}}$	$\sigma_{\text{FAP}}$
Fe I	0.015	3.45	-2	0.013±0.002	-4.81±0.72	12.39±1.69	1.19e-06	4.72
Fe II	0.125	4.60	-1	0.130±0.011	-0.75±0.37	8.54±0.87	9.72e-07	4.76
Cr II	0.120	3.69	-3	0.117±0.019	-3.40±0.42	5.31±0.99	2.47e-05	4.06
Na I	0.126	3.40	-2	0.139±0.015	-4.38±0.54	10.07±1.26	3.96e-06	4.47
Mg I	0.084	3.33	-3	0.062±0.005	-8.40±1.40	33.45±3.30	3.51e-05	3.98

**Table 1.** Summary of detected atomic species. Columns 1-4: Species name, peak relative absorption, signal-to-noise and location of the peak in the one-dimensional CCF. Columns 5-7: amplitude, centroid and FWHM of a Gaussian profile fit to the CCF feature, along with corresponding uncertainties. Columns 8 and 9: false-alarm-probabilities, and confidence level assuming Gaussianity.

lines reported in combined HARPS-N data (Casasayas-Barris et al. 2019) within  $\lesssim 2\sigma$ . Likewise, our Na I depth ( $0.139 \pm 0.015\%$ ) is comparable to the previously reported  $0.09 \pm 0.05\%$  combined strength of the Na D1 and D2 lines. In addition, all detected species have depths comparable to those found in the atmosphere of the ultra-hot Jupiter KELT-9 b (Hoeijmakers et al. 2019), but in contrast with KELT-9 b, this transit observation provides no evidence of absorption of Ti II, Sc II or Y II. We have fixed  $K_p$  at  $175 \text{ km s}^{-1}$ , consistent with the various optimal values of  $K_p$  found by Casasayas-Barris et al. (2019); Nugroho et al. (2020); Stangret et al. (2020). Variations of several  $\text{km s}^{-1}$  in  $K_p$  do not change the recovered signal amplitudes or confidence levels appreciably.

To explain this discrepancy, we note that there is a difference in equilibrium temperature of almost 2,000 K between M2 ( $T_{\text{eq}} \sim 2260 \text{ K}$ ) and the much hotter KELT-9 b

( $T_{\text{eq}} \sim 4050 \text{ K}$  (Gaudi et al. 2017)), so it is plausible that significant differences exist between the atmosphere chemistry and thermal structure of the atmospheres of these two planets. In addition, the present observations were obtained over the course of a single transit, whereas two transits of KELT-9 b were used by Hoeijmakers et al. (2019). As a result, the combined cross-correlation functions have lower signal-to-noise than what was achieved in the analysis of KELT-9 b, resulting in lower sensitivities to trace species like Sc II or Y II, which were also least strongly detected in the sample of Hoeijmakers et al. (2019).

With regards to the non-detection of Ti II that was strongly detected in KELT-9 b, it is worth noting that the equilibrium temperature of M2 is slightly below that of WASP-121 b ( $T_{\text{eq}} \sim 2358 \text{ K}$ ) for which TiO condensation has been observed to be important (Delrez et al. 2016; Evans et al. 2018).

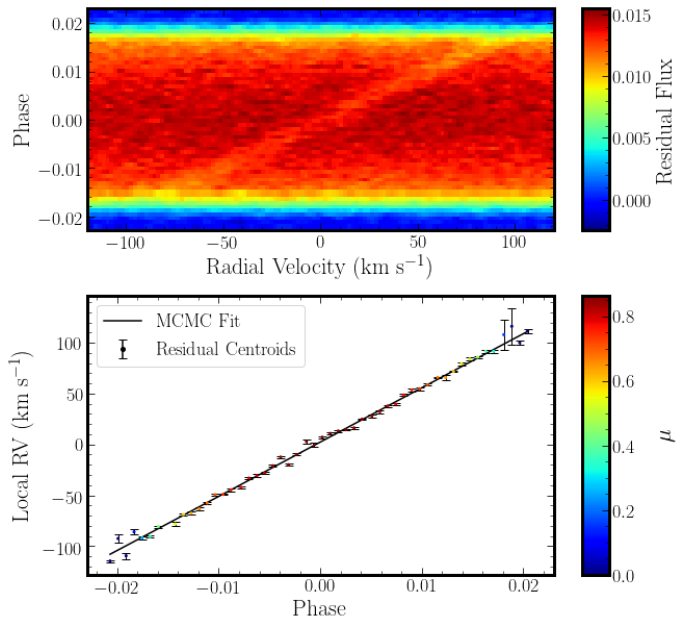


**Fig. 3.** *Top Panel:* The two-dimensional CCF obtained using the PHOENIX stellar template, normalized by the transit light-curve. *Bottom Panel:* The functional form of the time-dependent centroid velocity of the Doppler shadow is fit using an MCMC optimizer, providing posterior distributions of the system parameters (see Fig. A.1).

The peak locations of the CCF features generally suggest a blueshift of  $\sim -1$  to  $-9$  km s<sup>-1</sup>, which may be indicative of a day-to-night side wind or systematic errors in the determination of the systemic velocity, which can be difficult to constrain for fast-rotators (Hoeijmakers et al. 2019). However, recent works by Nugroho et al. (2020) and Stangret et al. (2020) also report blueshifts of the Fe I and Fe II signals of a few km s<sup>-1</sup>, with Fe II generally showing a smaller blueshift than Fe I. Therefore, the interpretation that atmospheric absorption lines are significantly blue-shifted appears to be robust across multiple independent studies, indicating the presence of a day-to-night side wind. This wind appears to affect Fe I and Fe II differently, suggesting a stratification of the atmosphere, as also hypothesised by Nugroho et al. (2020).

The CCF for Ti II exhibits a slight enhancement at  $0.0$  km s<sup>-1</sup> with a S/N  $\sim 2.4$ . While this peak is the highest in the one-dimensional CCF, we refrain from claiming a detection. All detections listed in Table 1 have S/N of at least 3.0, and correspond to the maximum in the one-dimensional CCF. These two criteria were not met by the CCF of any other species.

The absorption signature of Mg I appears significantly broader compared to the other species, with a measured FWHM of  $33.45 \pm 3.30$  km s<sup>-1</sup> versus  $\sim 10$  km s<sup>-1</sup> for the other species. On its own, the current data does not provide evidence to identify the cause of broadening processes that would act on Mg I specifically. However, we note that diverse broadening has also been observed in the transmission spectrum of KELT-9 b, with Na I and Mg I showing FWHMs of  $27.8 \pm 3.7$  and  $27.5 \pm 4.3$  respectively (Hoeijmakers et al. 2019) as opposed to values between 10 and 20 km s<sup>-1</sup> for other species. Assuming that line broadening is mainly due to atmospheric dynamics, differences in the line-widths of different species would suggest that certain

species may exist in distinct dynamical regimes in the upper atmospheres of ultra-hot Jupiters. This could include day-to-night side flows versus super-rotational jets (Showman et al. 2013; Louden & Wheatley 2015; Brogi et al. 2016) or radial outflows (Seidel et al. 2019). However, further analysis and observations will be needed to clarify the mechanism by which the absorption lines of certain species may be differentially broadened by these effects, and to what extent such processes are common among ultra-hot Jupiters.

## 4. Discussion & Conclusion

### 4.1. Bootstrap and Temporal Variation

The statistical treatment of the signatures as quoted above assumes that the noise in the cross-correlation function is normally distributed and uncorrelated. To determine the robustness of the detected signals, we determine false-alarm probabilities (FAP) using a bootstrap approach as follows. For a given species, we start with the two-dimensional, CCF time-series after removing the Doppler shadow. We randomly shuffle each row of the CCF, co-add in the rest-frame of the planet, fit a Gaussian profile at  $0.0$  km s<sup>-1</sup> (i.e. the center of the randomly shuffled rows), and record the fitted amplitude. This process is repeated 50,000 times to populate a random distribution of amplitudes. When fitting the Gaussian, we enforce a FWHM  $\geq 5$  km s<sup>-1</sup> and a centroid  $|\mu| \leq 20$  km s<sup>-1</sup>. By setting a minimum FWHM, we require that a spurious CCF enhancement must be sufficiently wide to qualify as a false-alarm. Narrower absorption line profiles would be inconsistent with the minimum width set by the rotation of the planet, assuming tidal locking. Indeed, all of the reported detections in Table 1 have FWHM  $> 5$  km s<sup>-1</sup>. Finally, we fit the tail of the amplitude distribution with a power law model, and extrapolate it to the detected signal’s strength. If we assume the distribution is Gaussian, the FAP can be converted to a  $\sigma$ -confidence level. The distribution of random amplitudes is shown in Fig. 5 for the case of Fe II. Distributions for other species are in the Appendix.

The FAP does not account for autocorrelation between absorption lines from a given species, or spurious correlations between lines from different species. Since several CCFs show strong spurious signals (offset from the  $0.0$  km s<sup>-1</sup> mark), we manually check the autocorrelation function of each model template. Additionally, we check the cross-correlation function between each template and Fe I and Fe II, since these species contribute a multitude of strong absorption lines. The peak in the Mg I CCF at  $+80$  km s<sup>-1</sup> is due to spurious correlation with a strong nearby Fe II line, also observed by Hoeijmakers et al. (2019). Fe II also produces a signal with Cr II near  $+50$  km s<sup>-1</sup>. Autocorrelations for the detected species do not produce significant spurious signals, and spurious correlations with Fe I are at much lower amplitude than the detections. Spurious features in CCFs of Na I near  $+90$  km s<sup>-1</sup>, Cr II near  $+20$  km s<sup>-1</sup>, and Ti II near  $+90$  km s<sup>-1</sup> and  $+170$  km s<sup>-1</sup> cannot be easily explained, and may result from noise in the two-dimensional CCF.

The measured planetary absorption signal appears to be stronger in the second half of the transit than it does in the first half. This is most evident in the upper-right panel of Fig. 4, where the signature of the Fe II line appears visible by eye during the later exposures of the observing

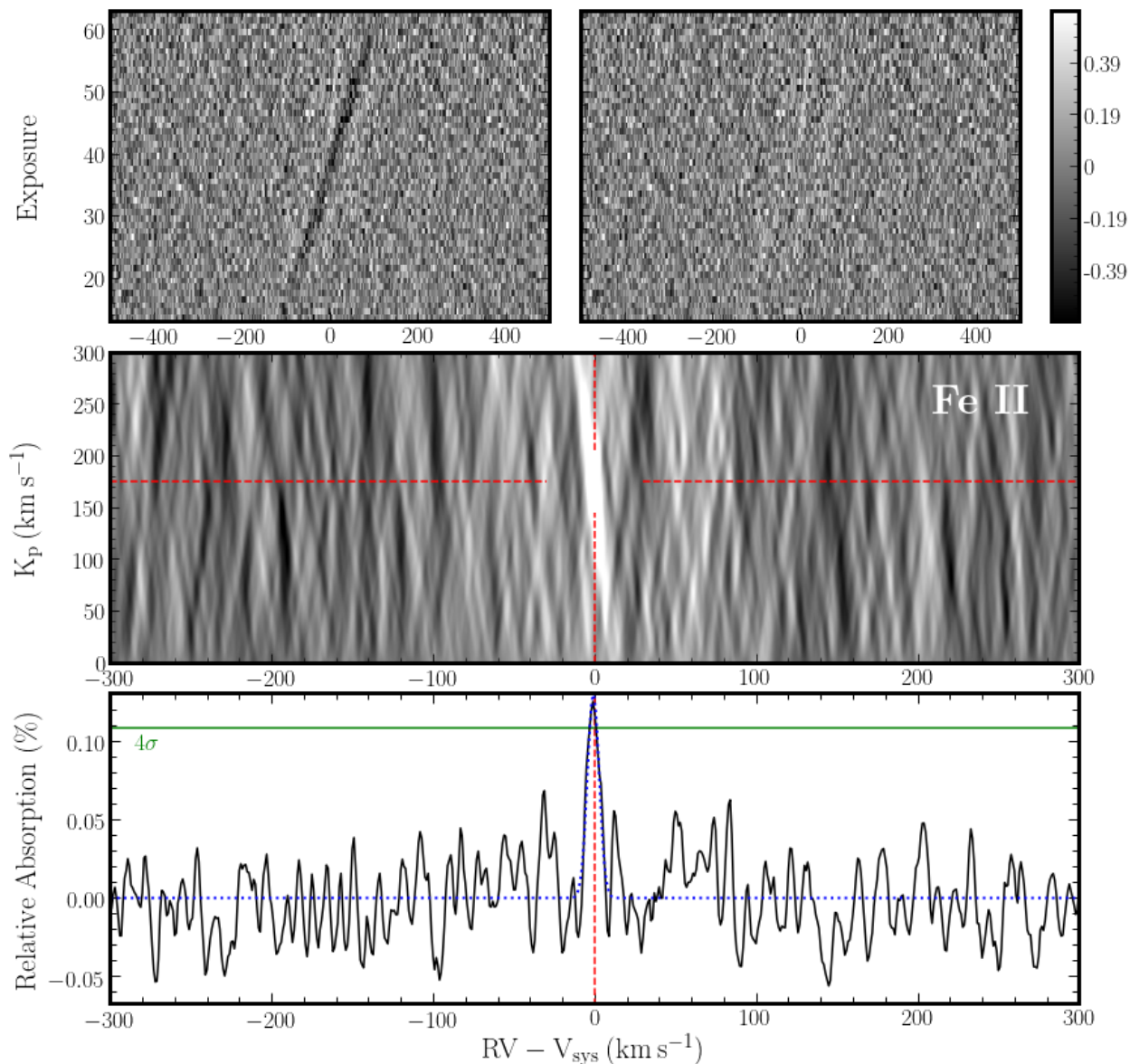


**Fig. 4.** Cross-correlation procedure and detection of Fe II in the transmission spectrum of MASCARA-2 b. *Upper panels:* two-dimensional cross-correlation with the Fe II template before (left) and after (right) correction of the Doppler shadow. *Middle panel:*  $K_p V_{\text{sys}}$  diagram. The red dashed lines indicate the expected location of the atmospheric signal. Because the data are shifted by the systemic velocity and Barycentric Earth Radial Velocity, the signal lies at approximately 0 along the x-axis. *Bottom panel:* Cross-correlation function co-added in the rest-frame of the planet. The green line marks  $4\times$  the standard deviation of the CCF. An enhancement is detected at the rest-frame velocity of the planet, which is modeled with a Gaussian profile (blue dotted line).

sequence. While this could be stochastic, particularly because this analysis is based on a single transit, it may instead be a physical effect related to the distribution of Fe II in the atmosphere of the planet, where it is present on the day-side near the evening (trailing) terminator that rotates into view towards the end of the transit, an effect that has recently been used to explain time-dependencies in the absorption spectrum of Fe I in the atmospheres of WASP-121 b (Bourrier et al. 2019) and WASP-76 b (Ehrenreich et al. 2020). We quantify this trend by fitting a Gaussian profile to the one-dimensional co-added CCF feature, using only the first and second halves of the in-transit exposures separately (Fig. 6). We take the difference between the two Gaussians’ amplitudes of Fe II (which shows the largest relative discrepancy between transit halves) and compare this

to differences that might arise by chance, given a signal that is uniform throughout the transit.

First, we add a Gaussian absorption line of identical amplitude and FWHM as the detected absorption line to each row of the two-dimensional CCF, thereby injecting an artificial signal of identical strength. The centroid is set by the corresponding phase, and a randomly selected  $0 < K_p < 300 \text{ km s}^{-1}$ , and  $-300 < V_{\text{sys}} < 300 \text{ km s}^{-1}$  (excluding  $-20 < V_{\text{sys}} < 20 \text{ km s}^{-1}$  to avoid overlap with the actual planet signal). We subsequently stack the two-dimensional CCF along the injected signal’s velocities, treating the first and second halves separately. We fit new Gaussians at the injected signal’s  $V_{\text{sys}}$  for each half, and record the difference in their amplitudes. We repeat this procedure 10,000 times, injecting and recovering a signal



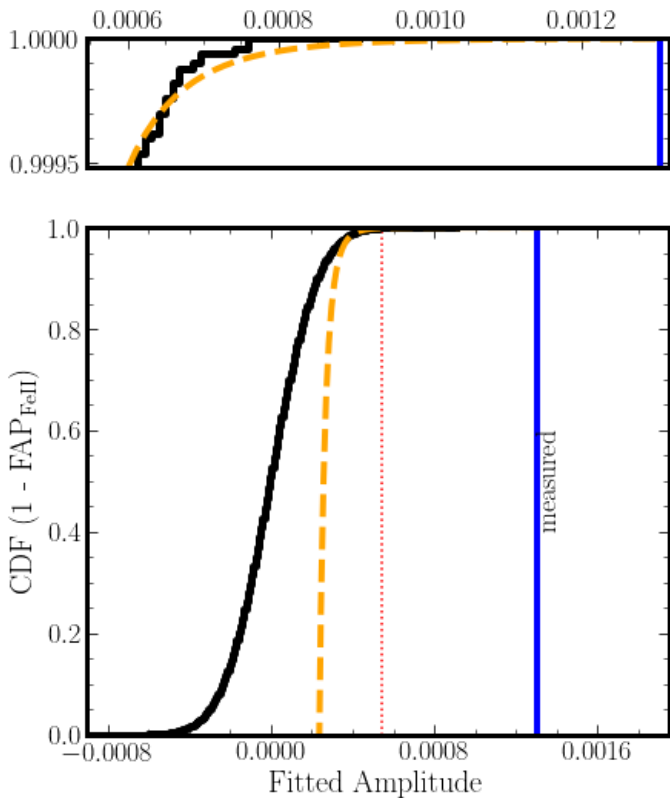


**Fig. 5.** Cumulative Distribution Function (CDF) of amplitudes of Gaussian fits to the randomly shuffled and stacked Fe II CCF. The black curve depicts the CDF. The blue solid line marks the strength of the Fe II detection. The dotted red-line marks three standard deviations from the distribution mean, after which the distribution is fitted with a powerlaw, shown as a the orange dashed line. The upper panel zooms in on the tail of the CDF for clarity.

along random paths in the two-dimensional CCF. Results are shown in Figure 7, where the observed difference or greater occurs in  $1.2 \times 10^{-3}$  of all cases. Assuming the distribution is Gaussian, the observed Fe II amplitude difference is at a  $2.7\sigma$  confidence level.

Variability of the depth of absorption features has been observed in the transmission spectra of KELT-9 b (Cauley et al. 2019) and currently most clearly in WASP-76 b (Ehrenreich et al. 2020). In the case of WASP-76 b, this is attributed to differences in chemical composition between the morning (leading) and evening (trailing) terminators, due to the offset of the substellar hot-spot towards the evening terminator. These observations show the appearance of a significant blue-shift as the evening twilight region rotates into view, which is explained by the rotation of the planet in combination with a day-to-night-side wind: The transmission spectrum of the leading terminator probes cool gas that streams from the night-side towards the hot day-side. Conversely, the trailing limb contains hot gas that was strongly irradiated on the day-side and is approaching the night-side where it cools down. However, in the case of M2 b, the absorption signal appears to be symmetric around  $0 \text{ km s}^{-1}$ , which may indicate that the chemistry at both terminators is more similar than for WASP-76 b. An increase in the absorption line (which in this data may amount to a factor of 2, see Fig. 7), may however be in-

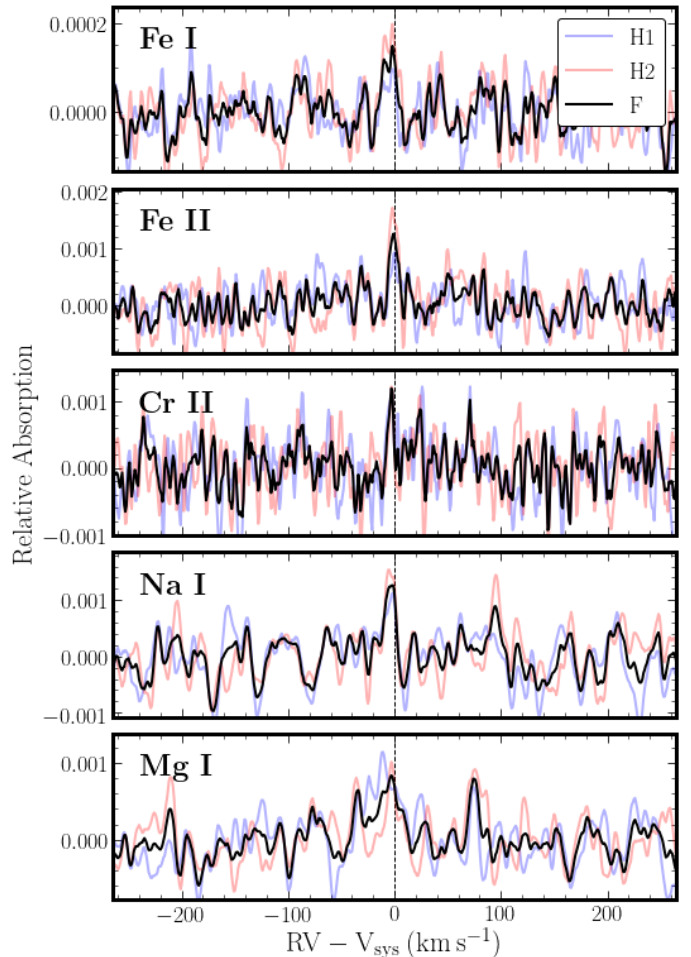


**Fig. 6.** Comparison of co-added CCF features using data from the first half of transit (blue curve), second half (red curve) and full transit (black curve), for each of the strongest species detections (Fe I, Fe II and Cr II). The legend denotes which in-transit exposures were used in the calculation (H1, H2, F denote first half of transit, second half of transit and full transit respectively). The dashed line indicates the expected location of the signal, at  $0.0 \text{ km s}^{-1}$  velocity offset.

dicative of a scale-height difference on both terminators, which could be caused by the temperature on the evening terminator being higher than on the morning terminator.

#### 4.2. Summary

In this paper we present detections of atomic metal absorption lines in the transmission spectrum of the ultra-hot Jupiter MASCARA-2 b (Lund et al. 2017; Talens et al. 2018). To this end, one transit of MASCARA-2 b was observed with EXPRES, the high-resolution optical spectrograph newly commissioned at the Lowell Discovery Telescope. We confirm previous detections of Fe I, Fe II and Na I (Casasayas-Barris et al. 2018, 2019; Nugroho et al. 2020; Stangret et al. 2020), and additionally find strong evidence for line absorption by atomic Mg I, and Cr II. All detected species appear to be blue-shifted, indicating the presence of a day-to-night side wind, also observed in previous studies (e.g. Nugroho et al. 2020; Stangret et al. 2020). Using the shape variation of the stellar absorption lines induced by the transiting planet (i.e. the Doppler

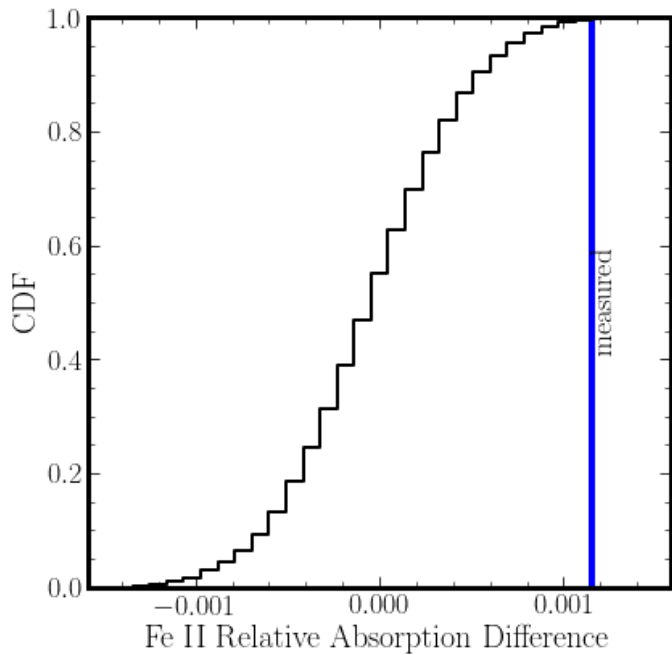


**Fig. 7.** Cumulative Distribution Function of the difference in amplitudes recovered from injecting an artificial Fe II signal, and recovering it in the first and second halves of transit separately. The vertical blue line marks the measured difference in amplitudes.

shadow), we constrain the projected spin-orbit misalignment to  $1.6 \pm 3.1$  degrees, consistent with an aligned orbit. The cross-correlation functions indicate hints of time-variability in the absorption strength of these species, albeit at a level of  $\lesssim 3\sigma$ . With a single transit, we cannot rule out that this variability is spurious. However, if it is astrophysical in origin, it potentially traces differential atmospheric structure between morning and evening terminators, reminiscent of what has recently been observed in the transmission spectrum of WASP-76 b (Ehrenreich et al. 2020). These results demonstrate the first spectroscopic observation of an exoplanet atmosphere with the EXPRES instrument, demonstrating its future potential for atmospheric characterisation.

*Acknowledgements.* This work was supported by the PlanetS National Centre of Competence in Research (NCCR) supported by the Swiss National Science Foundation (SNSF), the NSF under grants NSF MRI-1429365 and ATI-1509436 and by the European Research Council (ERC) under the European Union’s Horizon 2020 research and innovation programme (projects Four Aces and EXOKLEIN with grant agreement numbers 724427 and 771620, respectively). We acknowledge generous support for telescope time provided by the Heising-Simons Foundation and the Yale Astronomy Department. DAF and JMB wish to acknowledge support from an anonymous donation, which has also been used for telescope time. LLZ gratefully acknowledges support from the NSF GRFP. These results made use of the Lowell Discovery Telescope at Lowell Observatory. Lowell is a private, non-profit institution dedicated to astrophysical research and public appreciation of astronomy and operates the LDT in partnership with Boston University, the University of Maryland, the University of Toledo, Northern Arizona University and Yale University. We thank the Lowell Observatory astronomers and staff for their extraordinary support.

## References

Albrecht, S., Winn, J. N., Johnson, J. A., et al. 2012, *ApJ*, 757, 18

- Allart, R., Bourrier, V., Lovis, C., et al. 2019, *A&A*, 623, A58  
Allart, R., Lovis, C., Pino, L., et al. 2017, *A&A*, 606, A144  
Astropy Collaboration, Robitaille, T. P., Tollerud, E. J., et al. 2013, *A&A*, 558, A33  
Birkby, J. L. 2018, arXiv e-prints, arXiv:1806.04617  
Birkby, J. L., de Kok, R. J., Brogi, M., et al. 2013, *MNRAS*, 436, L35  
Birkby, J. L., de Kok, R. J., Brogi, M., Schwarzw, H., & Snellen, I. A. G. 2017, *AJ*, 153, 138  
Blackman, R. T., Ong, J. M. J., & Fischer, D. A. 2019, *AJ*, 158, 40  
Bourrier, V., Kitzmann, D., Kuntzer, T., et al. 2019, arXiv e-prints, arXiv:1909.03010  
Bourrier, V., Lecavelier des Etangs, A., Hébrard, G., et al. 2015, *A&A*, 579, A55  
Brogi, M., de Kok, R. J., Albrecht, S., et al. 2016, *ApJ*, 817, 106  
Brogi, M., Snellen, I. A. G., de Kok, R. J., et al. 2012, *Nature*, 486, 502  
Cabot, S. H. C., Madhusudhan, N., Hawker, G. A., & Gandhi, S. 2019, *MNRAS*, 482, 4422  
Casasayas-Barris, N., Pallé, E., Yan, F., et al. 2018, *A&A*, 616, A151  
Casasayas-Barris, N., Pallé, E., Yan, F., et al. 2019, *A&A*, 628, A9  
Caulley, P. W., Shkolnik, E. L., Ilyin, I., et al. 2019, *AJ*, 157, 69  
Cegla, H. M., Lovis, C., Bourrier, V., et al. 2016, *A&A*, 588, A127  
Claudi, R., Benatti, S., Carleo, I., et al. 2017, *European Physical Journal Plus*, 132, 364  
Collier Cameron, A., Bruce, V. A., Miller, G. R. M., TriAUD, A. H. M. J., & Queloz, D. 2010, *MNRAS*, 403, 151  
Cosentino, R., Lovis, C., Pepe, F., et al. 2012, *Society of Photo-Optical Instrumentation Engineers (SPIE) Conference Series*, Vol. 8446, Harps-N: the new planet hunter at TNG, 84461V  
Crossfield, I. J. M. 2015, *PASP*, 127, 941  
Delrez, L., Santerne, A., Almenara, J. M., et al. 2016, *MNRAS*, 458, 4025  
Ehrenreich, D., Lovis, C., Allart, R., et al. 2020, *Nature*  
Evans, T. M., Sing, D. K., Goyal, J. M., et al. 2018, *AJ*, 156, 283  
Fischer, D. A., Anglada-Escude, G., Arriagada, P., et al. 2016, *PASP*, 128, 066001  
Flagg, L., Johns-Krull, C. M., Nofi, L., et al. 2019, *ApJ*, 878, L37  
Foreman-Mackey, D., Hogg, D. W., Lang, D., & Goodman, J. 2013, *PASP*, 125, 306  
Gaudi, B. S., Stassun, K. G., Collins, K. A., et al. 2017, *Nature*, 546, 514  
Grimm, S. L. & Heng, K. 2015, *ApJ*, 808, 182  
Guilluy, G., Sozzetti, A., Brogi, M., et al. 2019, *A&A*, 625, A107  
Hawker, G. A., Madhusudhan, N., Cabot, S. H. C., & Gandhi, S. 2018, *ApJ*, 863, L11  
Heng, K. & Showman, A. P. 2015, *Annual Review of Earth and Planetary Sciences*, 43, 509  
Hoeijmakers, H. J., Ehrenreich, D., Heng, K., et al. 2018a, *Nature*, 560, 453  
Hoeijmakers, H. J., Ehrenreich, D., Kitzmann, D., et al. 2019, *A&A*, 627, A165  
Hoeijmakers, H. J., Snellen, I. A. G., & van Terwisga, S. E. 2018b, *A&A*, 610, A47  
Husser, T.-O., Wende-von Berg, S., Dreizler, S., et al. 2013, *A&A*, 553, A6  
Jensen, A. G., Redfield, S., Endl, M., et al. 2012, *ApJ*, 751, 86  
Khalafinejad, S., von Essen, C., Hoeijmakers, H. J., et al. 2017, *A&A*, 598, A131  
Levine, S. E., Bida, T. A., Chytlek, T., et al. 2012, *Society of Photo-Optical Instrumentation Engineers (SPIE) Conference Series*, Vol. 8444, Status and performance of the Discovery Channel Telescope during commissioning, 844419  
Lockwood, A. C., Johnson, J. A., Bender, C. F., et al. 2014, *ApJ*, 783, L29  
Louden, T. & Wheatley, P. J. 2015, *ApJ*, 814, L24  
Lund, M. B., Rodriguez, J. E., Zhou, G., et al. 2017, *AJ*, 154, 194  
Madhusudhan, N., Agúndez, M., Moses, J. I., & Hu, Y. 2016, *Space Sci. Rev.*, 205, 285  
Nugroho, S. K., Gibson, N. P., de Mooij, E. J. W., et al. 2020, arXiv e-prints, arXiv:2003.04856  
Nugroho, S. K., Kawahara, H., Masuda, K., et al. 2017, *AJ*, 154, 221  
Ohta, Y., Taruya, A., & Suto, Y. 2005, *ApJ*, 622, 1118  
Oliva, E., Sanna, N., Rainer, M., et al. 2018, in *Ground-based and Airborne Instrumentation for Astronomy VII*, ed. C. J. Evans, L. Simard, & H. Takami, Vol. 10702, *International Society for Optics and Photonics (SPIE)*, 2118 – 2130  
Pepe, F., Cristiani, S., Rebolo, R., et al. 2013, *The Messenger*, 153, 6  
Petersburg, R. R., Joel Ong, J. M., Zhao, L. L., et al. 2020, *AJ*, 159, 187  
Pino, L., Ehrenreich, D., Allart, R., et al. 2018, *A&A*, 619, A3

- Piskorz, D., Benneke, B., Crockett, N. R., et al. 2016, *ApJ*, 832, 131
- Price-Whelan, A. M., Sipőcz, B. M., Günther, H. M., et al. 2018, *AJ*, 156, 123
- Quirrenbach, A., Amado, P. J., Mandel, H., et al. 2010, *Society of Photo-Optical Instrumentation Engineers (SPIE) Conference Series*, Vol. 7735, CARMENES: Calar Alto high-resolution search for M dwarfs with exo-earths with a near-infrared Echelle spectrograph, 773513
- Redfield, S., Endl, M., Cochran, W. D., & Koesterke, L. 2008, *ApJ*, 673, L87
- Schlaufman, K. C. 2010, *ApJ*, 719, 602
- Seidel, J. V., Ehrenreich, D., Wyttenbach, A., et al. 2019, *A&A*, 623, A166
- Showman, A. P., Fortney, J. J., Lewis, N. K., & Shabram, M. 2013, *ApJ*, 762, 24
- Smette, A., Sana, H., Noll, S., et al. 2015, *A&A*, 576, A77
- Snellen, I. A. G., Albrecht, S., de Mooij, E. J. W., & Le Poole, R. S. 2008, *A&A*, 487, 357
- Snellen, I. A. G., de Kok, R. J., de Mooij, E. J. W., & Albrecht, S. 2010, *Nature*, 465, 1049
- Stangret, M., Casasayas-Barris, N., Pallé, E., et al. 2020, arXiv e-prints, arXiv:2003.04650
- Stock, J. W., Kitzmann, D., Patzer, A. B. C., & Sedlmayr, E. 2018, *MNRAS*, 479, 865
- Talens, G. J. J., Justesen, A. B., Albrecht, S., et al. 2018, *A&A*, 612, A57
- Thibault, S., Rabou, P., Donati, J.-F., et al. 2012, in *Proc. SPIE*, Vol. 8446, Ground-based and Airborne Instrumentation for Astronomy IV, 844630
- Thompson, S. J., Queloz, D., Baraffe, I., et al. 2016, in *Society of Photo-Optical Instrumentation Engineers (SPIE) Conference Series*, Vol. 9908, Proc. SPIE, 99086F
- Triaud, A. H. M. J. 2018, *The Rossiter-McLaughlin Effect in Exoplanet Research*, 2
- Turner, J. D., de Mooij, E. J. W., Jayawardhana, R., et al. 2020, *ApJ*, 888, L13
- Wildi, F., Blind, N., Reshetov, V., et al. 2017, in *Society of Photo-Optical Instrumentation Engineers (SPIE) Conference Series*, Vol. 10400, Society of Photo-Optical Instrumentation Engineers (SPIE) Conference Series, 1040018
- Winn, J. N., Fabrycky, D., Albrecht, S., & Johnson, J. A. 2010, *ApJ*, 718, L145
- Wright, J. T. 2018, *Radial Velocities as an Exoplanet Discovery Method*, 4
- Wyttenbach, A., Ehrenreich, D., Lovis, C., Udry, S., & Pepe, F. 2015, *A&A*, 577, A62
- Wyttenbach, A., Lovis, C., Ehrenreich, D., et al. 2017, *A&A*, 602, A36
- Yan, F. & Henning, T. 2018, *Nature Astronomy*, 2, 714

## **Appendix A: MCMC Results, Additional Figures**

Parameter	Symbol	Unit	MCMC Median	T18 (Prior)	L17
Scaled Semi-major Axis	$a/R_*$	-	$7.50 \pm 0.04$	$7.50 \pm 0.04$	$7.44^{+0.14}_{-0.13}$
Projected Oblliquity	$\lambda$	$^\circ$	$1.58^{+3.14}_{-3.12}$	$0.6 \pm 4$	$3.4 \pm 2.1$
Orbit Inclination	$i_p$	$^\circ$	$86.16 \pm 0.5$	$86.4^{+0.5}_{-0.4}$	$86.15^{+0.28}_{-0.27}$
Projected Stellar Rotation Speed	$v \sin i_*$	$\text{km s}^{-1}$	$113.50^{+0.77}_{-0.74}$	$114 \pm 3$	$115.9 \pm 3.4$
RV Offset	-	$\text{km s}^{-1}$	$0.7 \pm 3.1$	$0 \pm 5^*$	-

**Table A.1.** MCMC results for modelling of the Rossiter-McLaughlin effect. The model consists of the four parameters listed in column one, plus a global RV offset. The MCMC median values are listed in column four. Uncertainties correspond to the 16<sup>th</sup> and 84<sup>th</sup> percentiles. For comparison, we list literature values in column five, and their references in column six. T18 denotes Talens et al. (2018), and L17 denotes Lund et al. (2017). Asterisk (\*) indicates RV Offset prior not from literature.

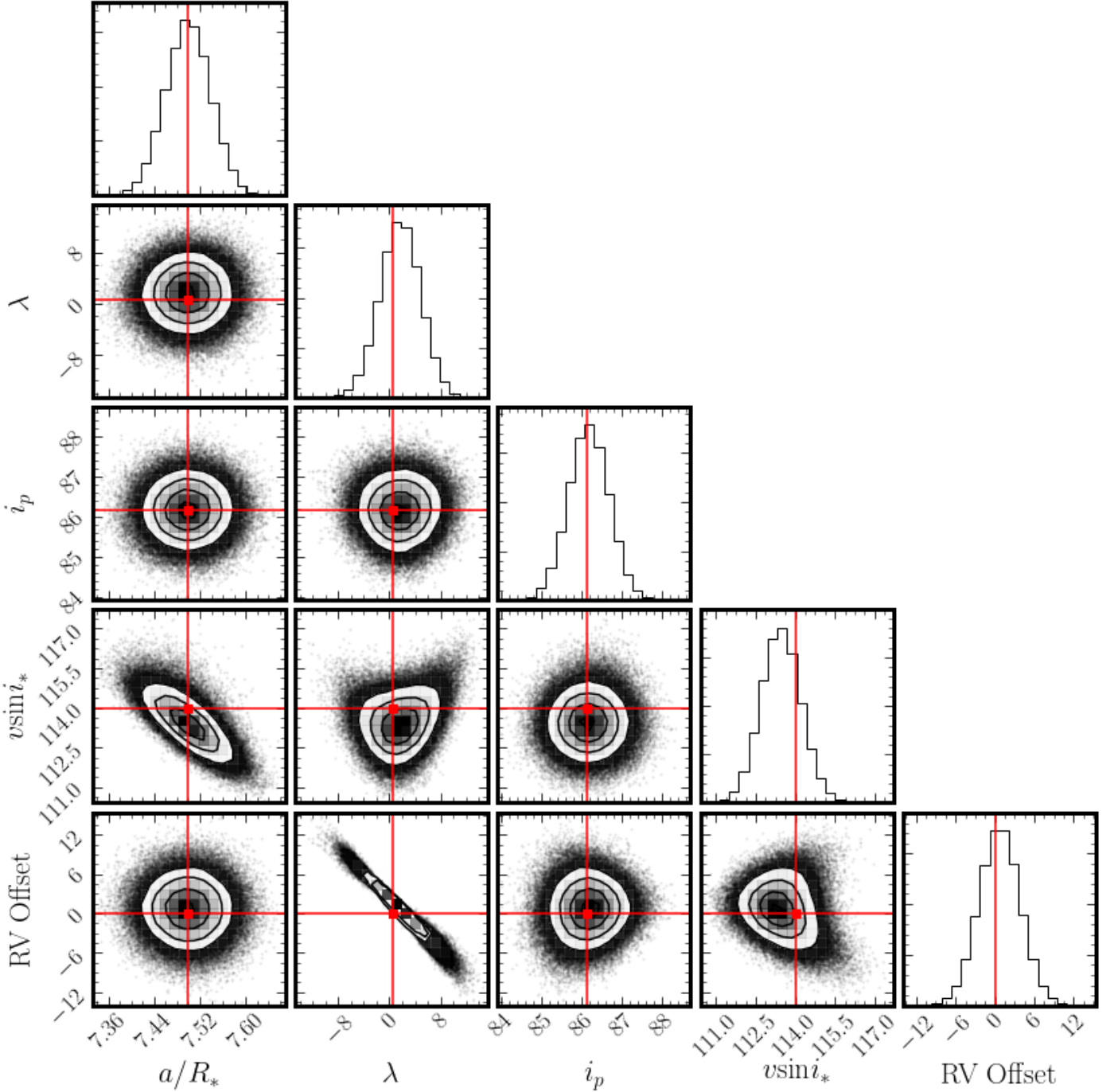


**Fig. A.1.** Correlation diagram from our MCMC fit to the observed Doppler shadow, as well as one-dimensional histograms. The model consists of five parameters: scaled semi-major axis ( $a/R_*$ ), projected obliquity ( $\lambda$ ), orbital inclination ( $i_p$ ), projected stellar rotation speed ( $v \sin i_*$ ), and a global RV offset. Red lines denote literature values for the parameters (Talens et al. 2018).

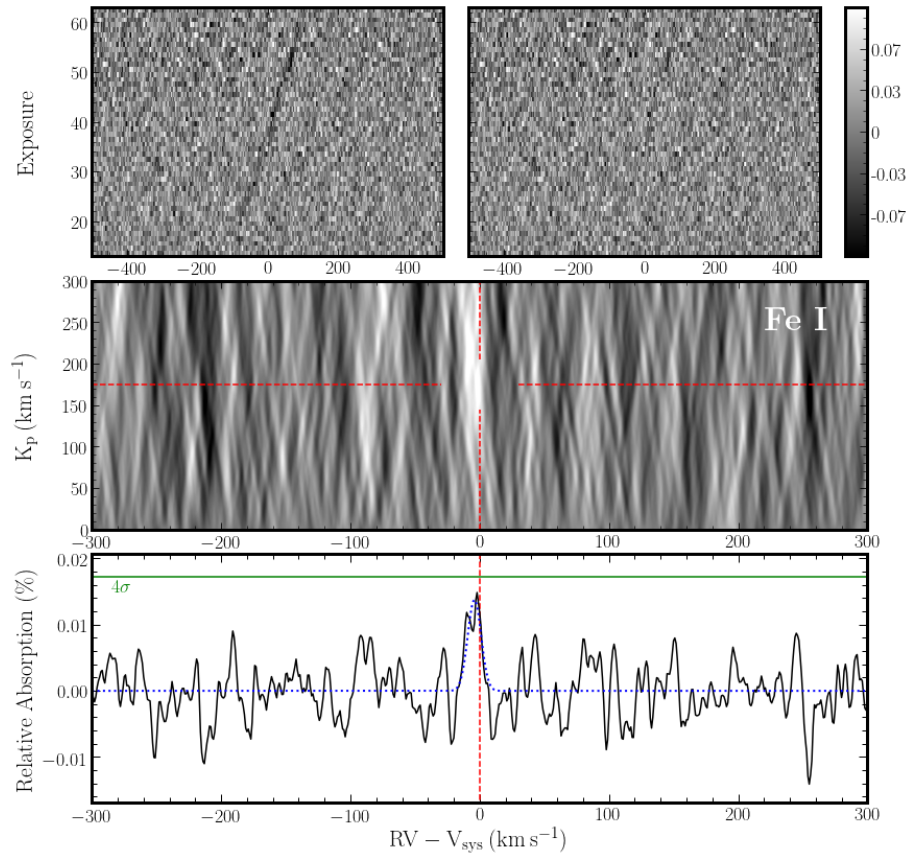


**Fig. A.2.** Same as Figure 4, depicting the cross-correlation process for Fe I. CCFs are in the rest-frame of the planet.

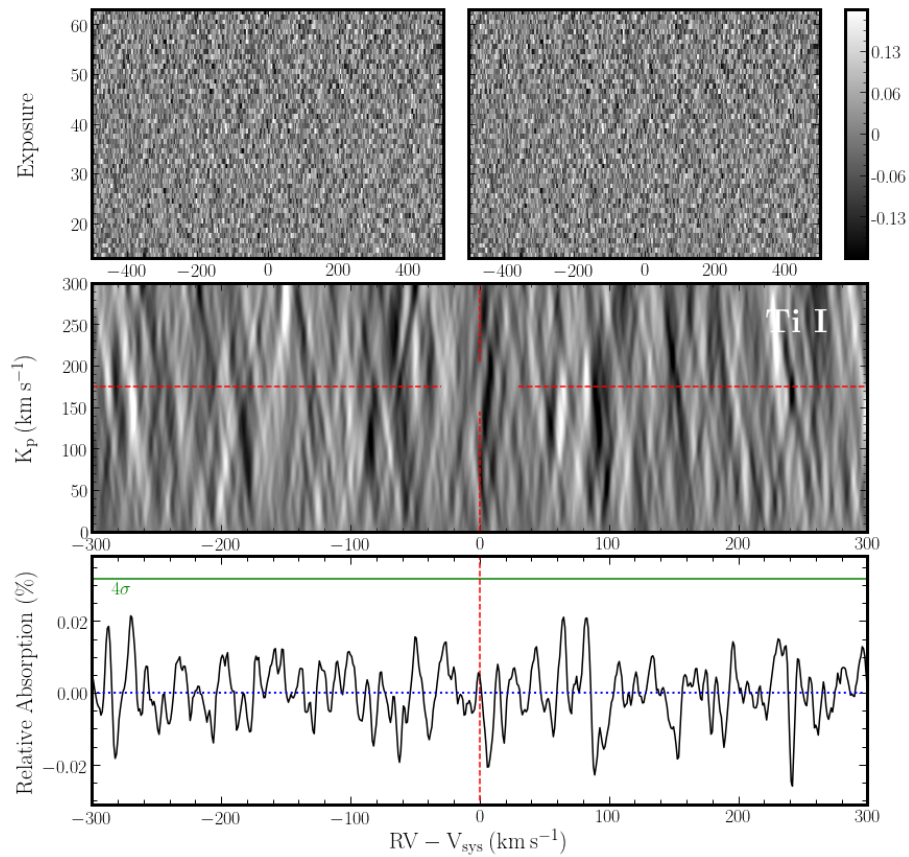


**Fig. A.3.** Same as Figure 4, depicting the cross-correlation process for Ti I. CCFs are in the rest-frame of the planet.

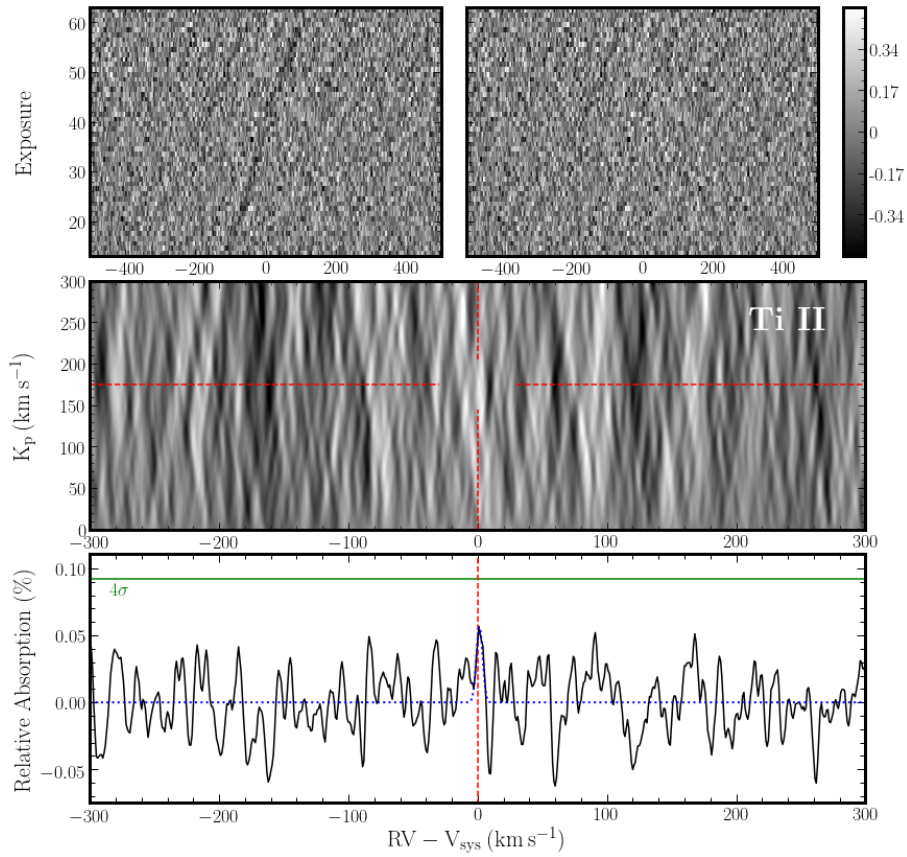


**Fig. A.4.** Same as Figure 4, depicting the cross-correlation process for Ti II. CCFs are in the rest-frame of the planet.

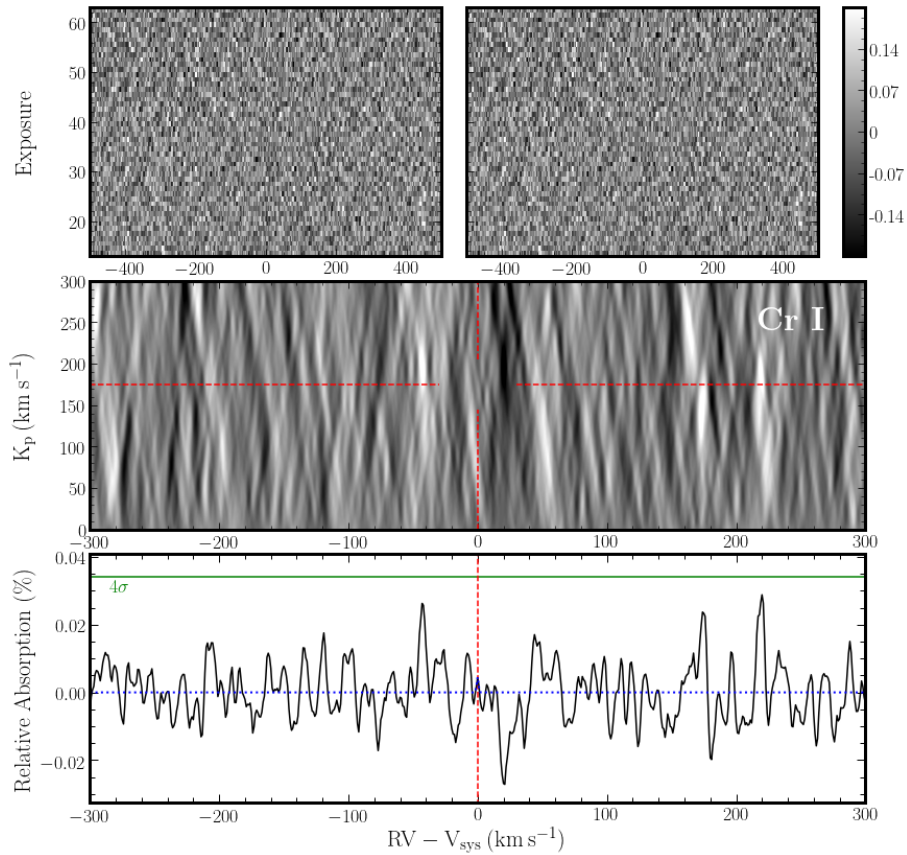


**Fig. A.5.** Same as Figure 4, depicting the cross-correlation process for Cr I. CCFs are in the rest-frame of the planet.

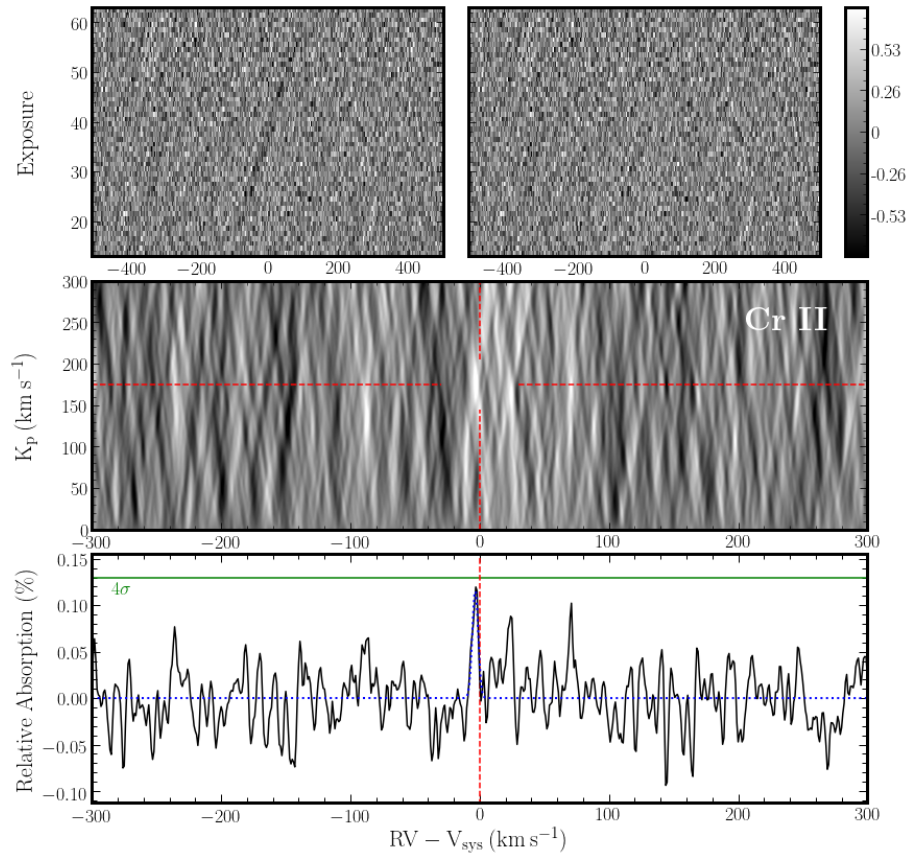


**Fig. A.6.** Same as Figure 4, depicting the cross-correlation process for Cr II. CCFs are in the rest-frame of the planet.

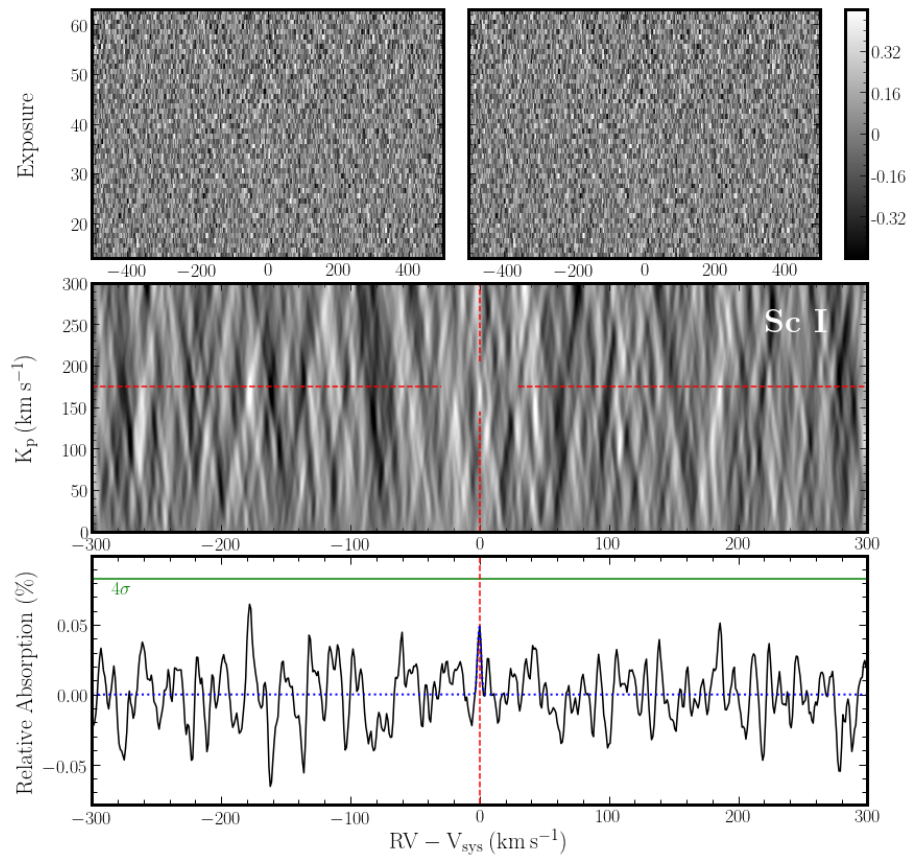


**Fig. A.7.** Same as Figure 4, depicting the cross-correlation process for Sc I. CCFs are in the rest-frame of the planet.



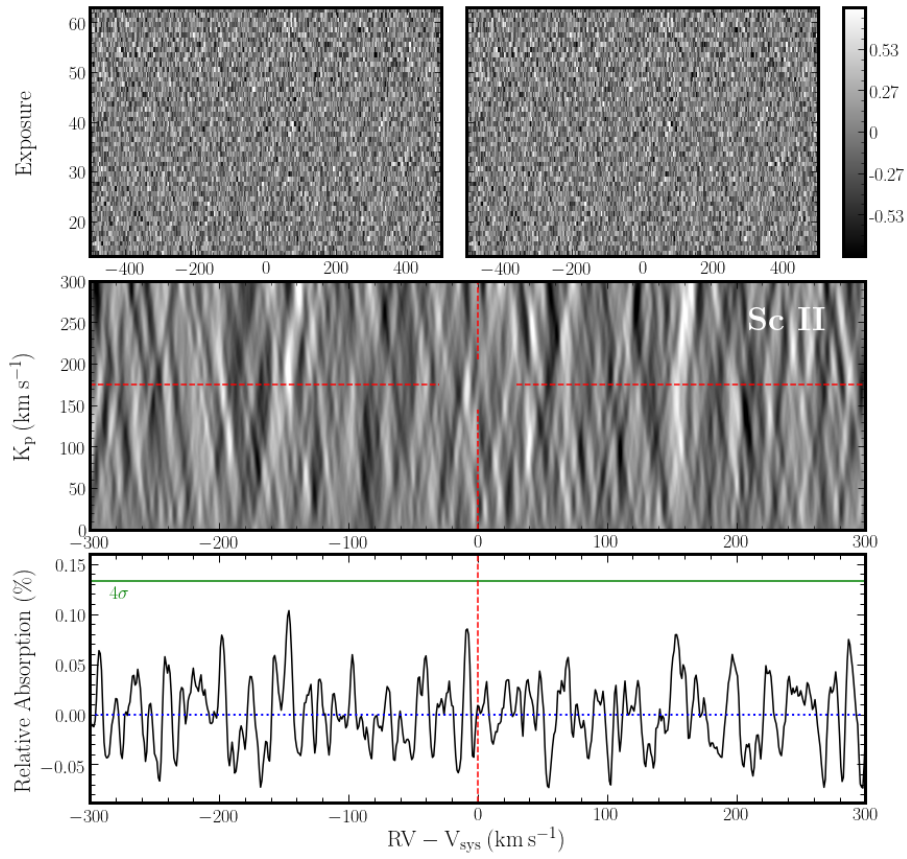


**Fig. A.8.** Same as Figure 4, depicting the cross-correlation process for Sc II. CCFs are in the rest-frame of the planet.

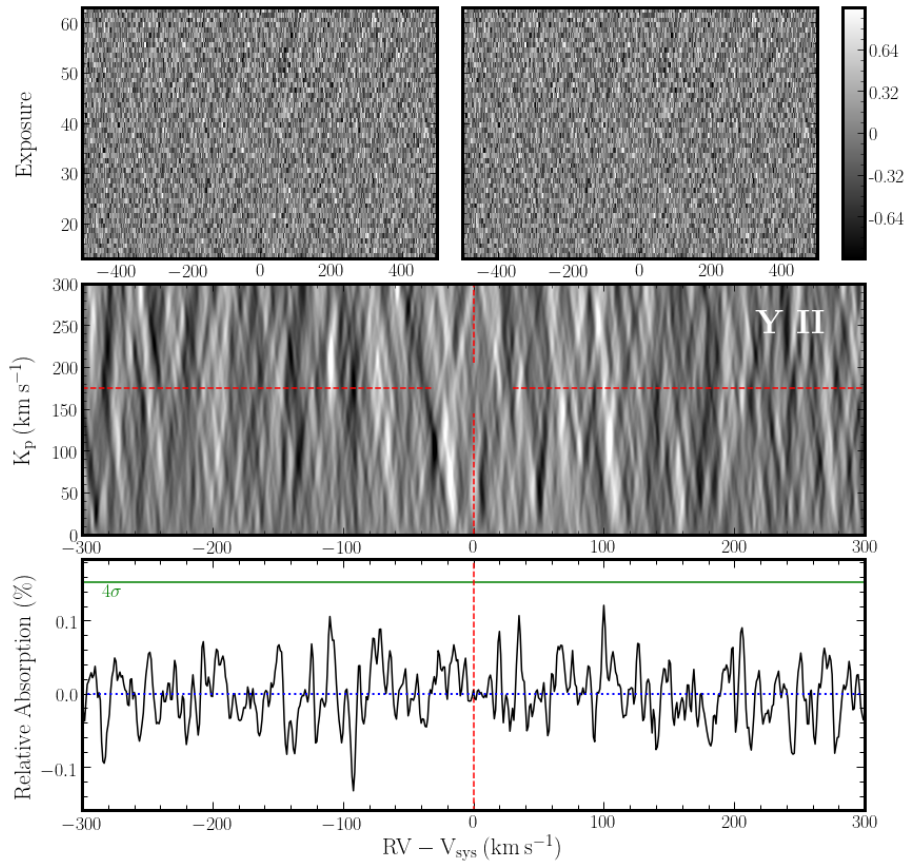


**Fig. A.9.** Same as Figure 4, depicting the cross-correlation process for Y II. CCFs are in the rest-frame of the planet.

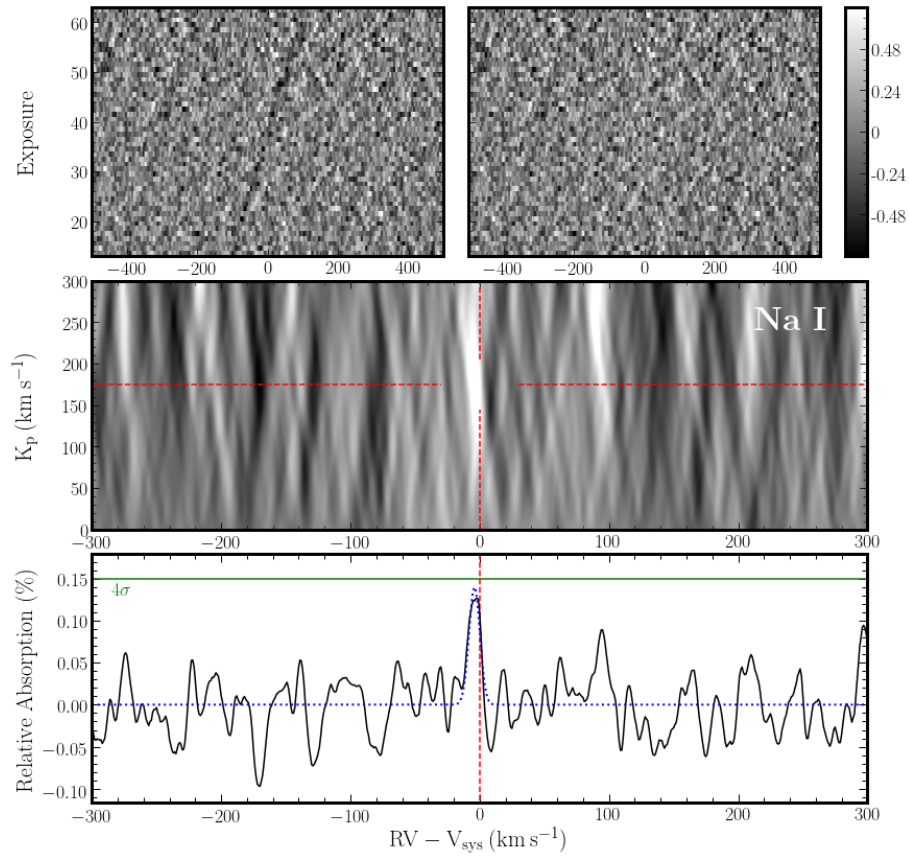


**Fig. A.10.** Same as Figure 4, depicting the cross-correlation process for Na I. CCFs are in the rest-frame of the planet.

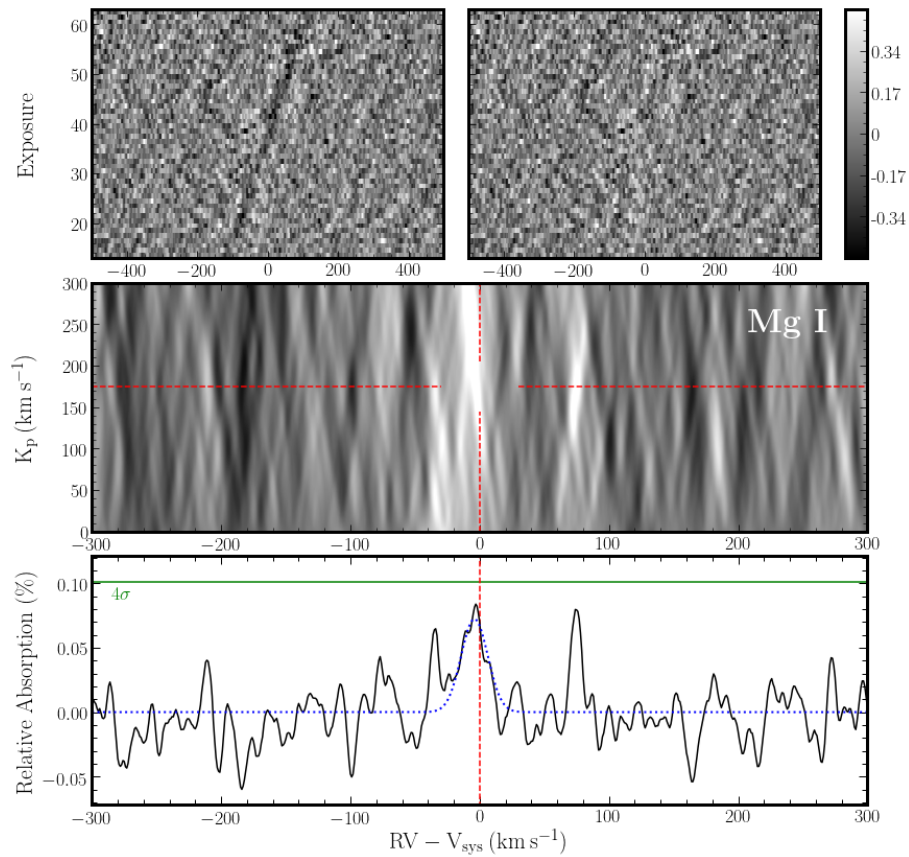


**Fig. A.11.** Same as Figure 4, depicting the cross-correlation process for Mg I. CCFs are in the rest-frame of the planet.

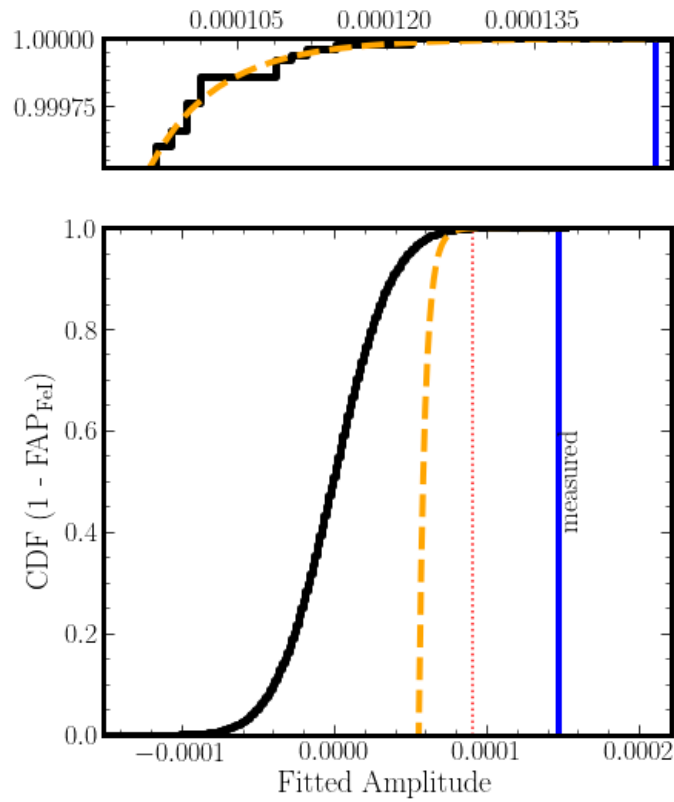


**Fig. A.12.** Same as Fig 5, except based on cross-correlation with the Fe I template. This plot shows the distribution of strengths of random signals generated by the CCFs, from which the FAP is derived.

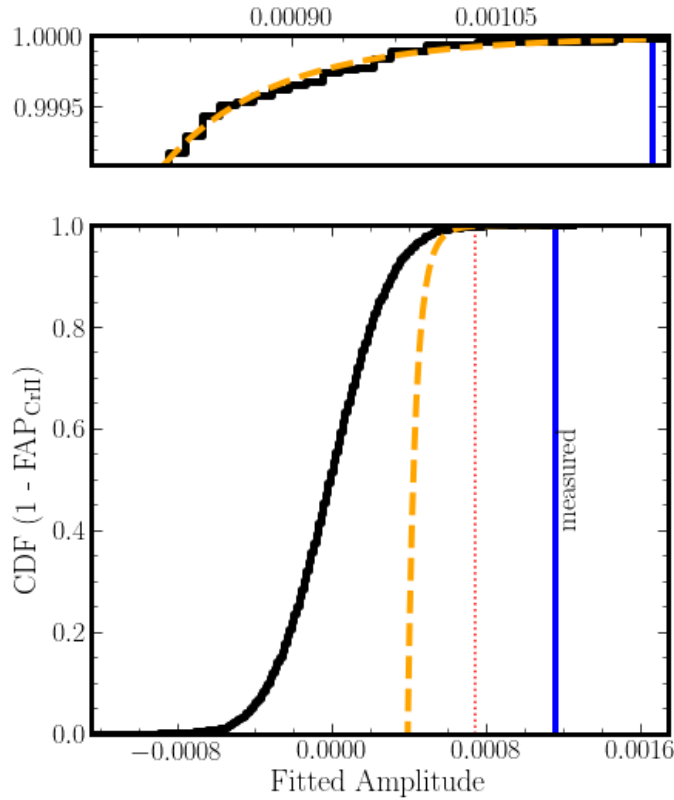


**Fig. A.13.** Same as Fig 5, except based on cross-correlation with the Cr II template. This plot shows the distribution of strengths of random signals generated by the CCFs, from which the FAP is derived.

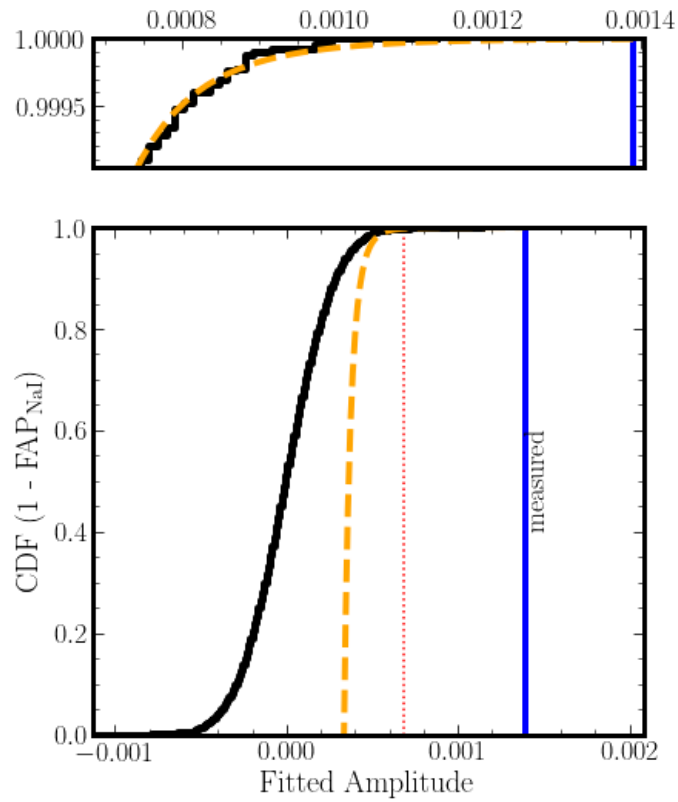


**Fig. A.14.** Same as Fig 5, except based on cross-correlation with the Na I template. This plot shows the distribution of strengths of random signals generated by the CCFs, from which the FAP is derived.

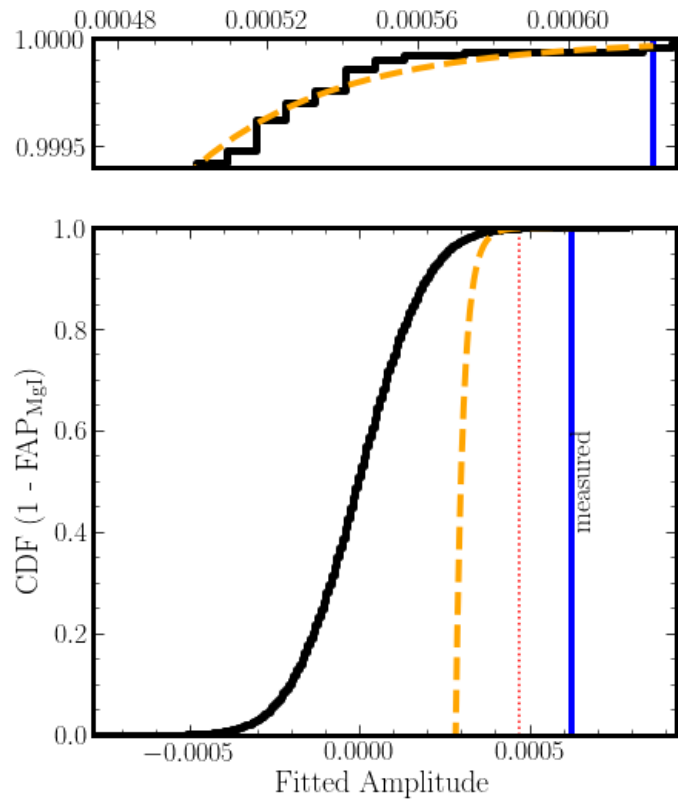


**Fig. A.15.** Same as Fig 5, except based on cross-correlation with the Mg I template. This plot shows the distribution of strengths of random signals generated by the CCFs, from which the FAP is derived.